

AD-A107 600

NAVAL RESEARCH LAB WASHINGTON DC

F/G 18/3

PRELIMINARY NUMERICAL SIMULATION OF IR STRUCTURE DEVELOPMENT IN--ETC(U)

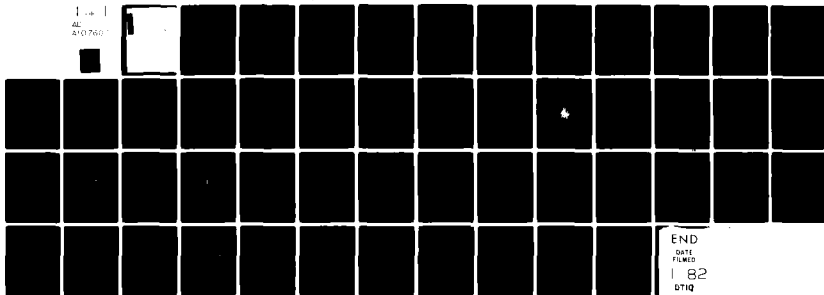
NOV 81 E HYMAN, M MULBRANDON, S L OSSAKOW

UNCLASSIFIED

NRL-MR-4659

NL

AL
A10760



AD A107600

SECURITY CLASSIFICATION OF THIS PAGE (When Data Entered)

REPORT DOCUMENTATION PAGE		READ INSTRUCTIONS BEFORE COMPLETING FORM
1. REPORT NUMBER NRL Memorandum Report 4659	2. GOVT ACCESSION NO.	3. RECIPIENT'S CATALOG NUMBER
4. TITLE (and Subtitle) PRELIMINARY NUMERICAL SIMULATION OF IR STRUCTURE DEVELOPMENT IN A HYPOTHETICAL URANIUM RELEASE	5. TYPE OF REPORT & PERIOD COVERED Interim report on a continuing NRL problem.	
7. AUTHOR(s) E. Hyman*, M. Mulbrandon, S. L. Ossakow, and B. E. McDonald**	6. CONTRACT OR GRANT NUMBER(s)	
9. PERFORMING ORGANIZATION NAME AND ADDRESS Naval Research Laboratory Washington, DC 20375	10. PROGRAM ELEMENT, PROJECT, TASK AREA & WORK UNIT NUMBERS 62074H; 47-0917-0-1	
11. CONTROLLING OFFICE NAME AND ADDRESS Defense Nuclear Agency Washington, DC 20305	12. REPORT DATE November 16, 1981	
	13. NUMBER OF PAGES 51	
14. MONITORING AGENCY NAME & ADDRESS (if different from Controlling Office)	15. SECURITY CLASS. (of this report) UNCLASSIFIED	
	15a. DECLASSIFICATION/DOWNGRADING SCHEDULE	
16. DISTRIBUTION STATEMENT (of this Report) Approved for public release; distribution unlimited.		
17. DISTRIBUTION STATEMENT (of the abstract entered in Block 20, if different from Report)		
18. SUPPLEMENTARY NOTES *Present address: Science Applications, Inc., McLean, VA 22102 **Present address: Naval Oceanographic Research and Development Activity, Bay St. Louis, MS 39520 This research was sponsored by the Defense Nuclear Agency under Subtask S99QAXHI, work unit 00001, and work unit title, "IR Structure."		
19. KEY WORDS (Continue on reverse side if necessary and identify by block number) IR Structure Power spectrum Uranium release Parallax effects Numerical simulation PHARO code Isophots LWIR		
20. ABSTRACT (Continue on reverse side if necessary and identify by block number) We present a three-dimensional (3D) simulation of a daytime hypothetical uranium release at 200 km altitude. Of interest is the LWIR emission from uranium oxide ions, induced by sunlight and earthshine. Assuming a one-level fluid and integrated Pedersen conductivity ratio (cloud to ambient) of 5, the cloud diffuses along the magnetic field in time and rapidly develops gradient drift striations transverse to the magnetic field and across the direction of the relative velocity of neutrals to ions. Using the PHARO code, we produce contour plots of radiance in the 11-14 μ region to simulate observations from various (Continues)		

DD FORM 1 JAN 73 1473

EDITION OF 1 NOV 63 IS OBSOLETE
S/N 0102-014-6601

SECURITY CLASSIFICATION OF THIS PAGE (When Data Entered)

20. ABSTRACT (Continued)

locations both along and transverse to the magnetic field. Contours of radiance vary in intensity and character from different vantage points. Power spectra are calculated to quantify the development of spatial irregularities in the radiance. We find parallax to be an important effect which alters both the appearance of the radiance contours and the spectral characteristics. This inherently 3D effect could not be observed in previous 2D simulations. Altering the distance from observer to cloud or changing slightly the direction of observation can produce drastic changes in the observations.

CONTENTS

I. INTRODUCTION	1
II. A HYPOTHETICAL EXPERIMENT	2
III. THE SIMULATION	4
IV. RESULTS	8
a. PHARO Plots	8
b. Power Spectra	11
c. Parallax Effects	14
V. SUMMARY	16
ACKNOWLEDGMENT	17
REFERENCES	45

A

PRELIMINARY NUMERICAL SIMULATION OF IR STRUCTURE DEVELOPMENT IN A HYPOTHETICAL URANIUM RELEASE

I. INTRODUCTION

The significance to U.S. defense systems of long wave infrared (LWIR) emissions from metallic oxides in the debris from a high altitude nuclear explosion (HANE) is an important unanswered question. Of most concern are structured or striating media since they degrade optical systems at intensities many orders of magnitude lower than smooth media. Those debris species which result in long lived ions are of most interest because they are the ones most likely to structure. For this reason uranium deserves careful scrutiny. Because of the low ionization potential of UO, uranium reacts with atomic oxygen via an associative ionization process to form UO^+ . Thus, this molecular ion is stable to dissociative recombination, and deionization requires a three body reaction. Uranium deposited in the high altitude atmosphere (>100 km) in a nuclear burst will, therefore, induce very long lived ionization. The emission characteristics of UO^+ have not been measured, although on general theoretical grounds a very large line density is expected in the $11\text{-}14\mu$ region. A laboratory experiment to measure the UO^+ spectrum (wavelengths and band strengths) in this region of the LWIR has been described by Bien.⁽¹⁾ It has not yet been carried out.

Because of the potential importance of uranium debris from HANE events in the performance of defense optical systems,

Manuscript submitted August 31, 1981.

the RAAE Division of the Defense Nuclear Agency has suggested that numerical simulations be performed to model high altitude uranium releases. Based on reasonable estimates of oscillator strengths for transitions in the LWIR, these simulations will predict structuring characteristics of the hypothetical plasma cloud released in the ionosphere. In this paper we will present results of a three dimensional simulation of a uranium release. Using the PHARO code we will show plots of radiance ($\text{watts/cm}^2 \text{ster}$) in the $11\text{-}14\mu$ region as a function of time, (assuming the emission to be optically thin), viewing both along and transverse to the magnetic field. These plots will show the development of structure in time. In addition, we will show the power spectra for the structure, giving the distribution of spatial wavelengths in the emitting band. Parallax effects will also be described.

II. HYPOTHETICAL EXPERIMENT

We will simulate a hypothetical release based on the parameters presented at the DNA Infrared Program Meeting at the Naval Research Laboratory in January 1980 by W. Reidy.⁽²⁾ A release at 200 km altitude in daylight with an atomic uranium content of 2 kgm ($\sim 5 \times 10^{24}$ atoms) is modeled. Initially the uranium vapor will expand radially with a thermal velocity somewhat less than 1 km/sec. The expanding uranium vapor would be slowed when it has interacted with an equal mass of the atmosphere (~ 1.2 km). However, before this occurs it will interact with an equal number of atomic oxygen atoms ($\sim .75$ km). Assuming an oxygen density $\sim 3 \times 10^9 \text{cm}^{-3}$ and a reaction rate coefficient

of $4 \times 10^{-10} \text{ cm}^3/\text{sec}$,⁽³⁾ the ionization will occur with an e-folding time of ~ 0.8 sec. This will restrict further growth of the cloud transverse to the magnetic field, and the cloud will initially develop a sausage-like shape with a radial dimension transverse to the magnetic field ~ 0.75 km. However, $\vec{E} \times \vec{B}$ convection will elongate the cloud in the direction of the relative velocity of the neutral atmosphere to the ion cloud, and will narrow it in the other direction transverse to the magnetic field.⁽⁴⁾

Because of the presence in the normal atmosphere at 200 km of a substantial amount of molecular oxygen, which may not be present in the nuclear disturbed atmosphere, a further reaction will occur: UO^+ will react with O_2 to form UO_2^+ . Assuming a reaction coefficient of $2 \times 10^{-9} \text{ cm}^3/\text{sec}$ ⁽⁵⁾ and an O_2 density of $\sim 4 \times 10^8 \text{ cm}^{-3}$ the e-folding time for conversion of UO^+ to UO_2^+ is just 1.2 sec. Thus, after the first several seconds the predominant ion will be UO_2^+ . This will have little effect on the dynamics and structuring of the ion cloud but the LWIR spectrum will be different, of course. Because in the nuclear case the O_2 molecules may be dissociated, the transition from UO^+ to UO_2^+ may take much longer. On the other hand, even in a high altitude burst much of the debris will typically be deposited at lower altitudes (~ 100 km) where there will be large amounts of O_2 .

Metal oxides are excited from the ground state to higher electronic levels by visible radiation from sunlight. These

excited levels rapidly decay, in general, to excited vibrational levels of the ground electronic state which radiate in the LWIR. In addition, there is direct excitation of vibrational levels caused by earthshine at LWIR wavelengths, leading to LWIR emission as these levels decay. Typical emission rates for metal oxides in the LWIR are $\sim 10^{-2}$ photons/molecule/sec due to earthshine, and $\sim 10^{-1}$ photons/molecule/sec due to sunlight.⁽⁶⁾ There has been some speculation that the emission rates for UO^+ and UO_2^+ may be substantially higher than these values⁽⁷⁾ because of the presence of low-lying electronic levels, but that has not been established. In the case of aluminum oxide the rate is ~ 2 photons/molecule/sec both for sunlight and for earthshine. LWIR emission is expected to be in the 11-14 μ region but the results in this paper do not depend on this specific wavelength interval.

III. THE SIMULATION

The model assumes a one ionic species, one-level fluid and follows the analysis used for the Avefria barium cloud releases.⁽⁸⁾ The conductivity ratio (UO^+ plasma cloud to background ionosphere Pedersen conductivity ratio), as defined in Reference 8, is taken to be 5 which is based on an assumption of 30% efficiency of vaporization of the uranium. Briefly, the conductivity ratio 5 was obtained as follows. The 5×10^{24} atoms of U was assumed to be 30% vaporized and the resulting UO^+ was gaussianly distributed over a sphere, with a gaussian radius of 0.75 km. Using a UO^+ ion-neutral collision-frequency (ν_{in}) of 0.2 s^{-1} and a gyro-frequency (Ω_i) of 18.8 s^{-1} , the integrated Pedersen conductivity of the UO^+ cloud was found to be 30 mhos. For the daytime high

latitude ionosphere, a value of 6 mhos for the integrated Pedersen conductivity was taken.

The altitudes and sizes of the ionized clouds are similar in the two releases as are the striation formation mechanisms and lead to the rapid development of gradient drift striations. Whereas, in the Avefria simulation, however, the F region ionospheric plasma cloud was reduced to two dimensions (transverse to the magnetic field) by performing field-line-integrations over the Pedersen conductivity, here in the model this is not done and the cloud also diffuses in time along the magnetic field, providing a three dimensional simulation. This enables one to view the cloud, using the PHARO code,⁽⁹⁾ from an arbitrary direction and to automatically incorporate any effects of parallax due to the three-dimensionality of the cloud. A PHARO plot is obtained by summing the volume emission rates along an array of rays originating at the camera location. A 2D array of radiance values is determined, from which a contour plot of the radiance is constructed.

Thus, the cloud is spherical for the first few seconds until it becomes ionized. From then on, after this time t_i , diffusion transverse to the magnetic field can be neglected. Along the magnetic field, we assume an initial density distribution $n(t_i) \sim \exp(-z^2/L^2)$, where z is the coordinate along the magnetic field (\underline{B}) direction and $L \sim .75$ km. With a parallel to

B diffusion constant $K_{\parallel} = c_s^2 / v_{in}$, where $c_s \sim .3$ km/sec and $v_{in}(UO^+) \sim .2 \text{ sec}^{-1}$, we have $K_{\parallel} \sim 4.15 \times 10^{-1} \text{ km}^2/\text{sec}$. The density diffuses in time according to

$$\frac{\partial n}{\partial t} = K_{\parallel} \frac{\partial^2 n}{\partial z^2} \quad (1)$$

At time t then, we will have

$$n(t, z) \propto \left[\frac{1}{1 + b(t-t_i)} \right]^{1/2} \exp \left(- \frac{z^2}{L^2} \left[\frac{1}{1 + b(t-t_i)} \right] \right) \quad (2)$$

with $b = 4K_{\parallel} / L^2 \sim 3.2 \text{ sec}^{-1}$.

The above analysis is strictly correct only for a uniform atmosphere. For a release in equatorial regions the z direction is horizontal and there is no problem. At high latitudes, where the magnetic field is nearly vertical, diffusion will be significantly faster in the upward direction than in the downward direction. Now, the diffusion scale size grows like the square root of the time and at 200 km is ~ 13.4 km at 100 sec. Therefore, at times of the

order of 100 sec this effect is not major (atmospheric scale size at 200 km \sim 43 km). We have, for this reason, not corrected for this effect in our simulation.

The above analysis is performed while simultaneously following the perpendicular motion and structuring of the UO^+ plasma cloud according to the one-level set of equations⁽⁸⁾

$$\frac{\partial \Sigma}{\partial t} = - \nabla_{\perp} \cdot (\Sigma \underline{V}) + \nabla_{\perp} \cdot (K_{\perp} \nabla_{\perp} \Sigma) \quad (3)$$

$$\underline{V} = - \frac{c}{B} \nabla_{\perp} \phi \times \underline{e} \quad (4)$$

$$\nabla_{\perp} \cdot (\Sigma \nabla_{\perp} \phi) = \underline{E}_0 \cdot \nabla_{\perp} \Sigma \quad (5)$$

where Σ , \underline{V} , K_{\perp} , ϕ , B and \underline{E}_0 are the integrated plasma cloud (UO^+) Pedersen conductivity ($\Sigma = \int \sigma_p(x, y, z) dz$, where σ_p is the Pedersen conductivity) and is a function of x, y (coordinates perpendicular to \underline{B}), perpendicular plasma velocity, relative to the ambient perpendicular plasma drift, the cross-field ($\perp \underline{B}$) diffusion coefficient, the cloud-induced potential, magnetic field strength, and ambient perpendicular electric field in the rest frame of the uniform neutral flow, respectively and the electrostatic approximation ($\underline{E} = \underline{E}_0 - \nabla_{\perp} \phi$) has been made. In addition⁽⁸⁾ $K_{\perp} = (2kT/m_i)(\nu_{en} + \nu_{ei}/\Omega_e \Omega_i)$ where k , T , m_i , ν_{en} , ν_{ei} , Ω_e and Ω_i are Boltzmann's constant, the plasma temperature, ion mass, electron-neutral collision frequency, electron-ion collision frequency, electron gyrofrequency and ion gyrofrequency,

respectively. Values of $E_0 = 5\text{mV/m}$, $B = 0.5$ gauss (and resulting in a cE_0/B velocity of 100 m/s), and $K_{\perp} \sim 1\text{ m}^2/\text{sec}$ were chosen for the simulations. The computational mesh consisted of 162×82 grid points in the x and y directions (see Figure 1). The plasma density distribution $n(x,y)$ at each time was unfolded from (3) - (5) by distributing the density along z according to the gaussian (with a time dependent gaussian length) given by (1) and (2), using $\phi_{in}(UO^+)$ and $\phi_i(UO^+)$, integrating over z and setting the resultant integral equal to $\Sigma(x,y)$.

In Figure 1 we indicate the coordinate system fixed in the ionized cloud, and illustrate the formation of striations transverse to the magnetic field, B , and across the direction of the relative velocity of the neutral atmosphere, v_n , to the ionized plasma. (In this system $\underline{E}_0 \times \underline{B}$ would be in the $-x$ direction). The calculational mesh follows the striating edge and has an outflow boundary condition on the negative x boundary. Thus, in time more and more ions are lost from the calculation out of the "tail". Figure 1 also exhibits the locations of 3 potential observation directions for infrared detectors (cameras). In the next section we will show plots of ir emission contours as observed from each of the camera locations. The emission rate is assumed to be $0.11\text{ photons/ion/sec}$ in the $11\text{-}14\mu$ band.

IV. RESULTS

a. PHARO Plots

Figures 2-8 show the contours of radiance in $\text{watts/cm}^2/\text{ster}$

at several times as observed from camera 1, placed a distance away of 200 km. Camera 1 looks along the magnetic field. Figure 2 shows a PHARO plot of the radiance 60 sec after the release. The abscissa and ordinate are in degrees and are respectively along the x and y directions in the coordinate system of Figure 1. An 82 x 82 mesh has been used in the PHARO part of the calculation in the camera plane of view. The contour values, defined in the headings of the plot, potentially range from 1.125×10^{-7} watts/cm² ster, (the "9" contour) to 0.0 (the "0" contour) in steps of 1.25×10^{-8} watts/cm² ster. The largest contour appearing in Figure 2 is the "8" contour which represents a radiance of 1.00×10^{-7} watts/cm² ster. A key at the bottom of the plot gives the value of some of the contours in watts/cm² ster. At 60 sec there is no sign of the fingering behavior which becomes so evident at later times. In Figure 3, 80 sec, the striating behavior has clearly begun developing. The structuring intensifies at 100, 120, 140, 160 and 180 sec shown in Figures 4, 5, 6, 7 and 8 respectively. The overall radiance has not diminished with time.

Camera 2 looks along the relative velocity vector of the neutral atmosphere and the ion cloud from a distance of 200 km. In Figure 9 we exhibit the PHARO plot at 140 sec as observed from camera 2 with a sufficiently large field of view that the entire cloud is in view. While this plot is useful to exhibit the entire cloud, there is not enough resolution to distinguish the contours.

For this, we return to the high resolution in Figure 10, which is at 60 sec. Only a portion of the cloud is in view here, of course. The magnetic field in Figure 10 is along the ordinate, and the abscissa is the y coordinate of Figure 1. Here the maximum contour value observed is 1.0×10^{-8} watts/cm² ster. The values of radiance determined from camera 2 are substantially lower than those from camera 1 since from this vantage point lines of sight do not pass through as much of the cloud as in the end view observed by camera 1. Furthermore, from camera 2 we are looking up the "tail", along the x-direction, and, as we pointed out, some of the ions have left the calculational mesh. This means that not only are the radiance levels too small as observed from this direction, but any nonuniformity in the "tail" has been lost. On the other hand, there is no fine structure lost, as this is all in the leading edge. Our calculations indicate that approximately 1/3 of the ions have left the mesh by 140 sec.

Note the near perfect symmetry at 60 sec, corresponding to the symmetry observed from camera 1 at this time. In Figures 11-14 we observe the changes in time from the camera 2 vantage point. At 100 sec, Figure 11, we see the maximum contour begin to shift to the left, corresponding to the maximum in Figure 4 shifting downward. A relative minimum forms just to the right of the central vertical axis corresponding to the depression in Figure 4 just above the central horizontal axis. These effects become more pronounced at succeeding times. Particularly interesting from

this direction is the alternation in intensities as we scan horizontally across the field of view (Figures 12-14). There is a gradual reduction with time in the radiance, also, as more of the cloud diffuses along the magnetic field out of the field of view, and, also, out of the calculational mesh (negative x boundary). The former is a real physical effect, the latter an artifact of the calculation.

Camera 3 looks in the direction transverse to the magnetic field and to the drift direction from a distance of 200 km. Again, in these views (Figures 15-19) not all of the cloud is included. The ordinate is along the magnetic field (z) and the abscissa is along the relative velocity (x). The steep gradients at the left of Figure 15 correspond to those on the right in Figure 2. As from camera 2, the radiance decreases with time as the cloud diffuses out of the field of view but there is no loss from missing ions, as the "tail" is not in the field of view of camera 3. Here the structuring leads to an appearance significantly distinct from either of the other two views.

b. Power Spectra

Spatial irregularity power spectra have been produced for each camera view. For example, consider the radiance as viewed from camera 1 at a distance of 200 km at 140 sec (Figure 6). Using a mesh dimension of 82×82 we construct a two dimensional (2D) power spectrum. This is converted to two one dimensional spectra: the x power spectrum is a result of integrating over the y components of the wavenumber (k_y) of the 2D power spectrum; the

y power spectrum comes from integrating over the x components (k_x). Typical results are shown in Figures 20 and 21. The power scale on the ordinate is in units of the logarithm of the square of the radiance. The abscissa has two scales: (1) the logarithm of the spatial wavelength in km, and (2) the logarithm of the mode number, k/k_1 , where $k_1 = 2\pi/D$. In the y direction D is the system size = 2.7km. By the system size we mean the distance across the field of view based on the distance between the camera and the cloud, and neglecting the dimensions of the cloud. In the x direction D is twice the system size, because of the Neumann boundary condition in x.

A typical power spectrum plot can be conveniently divided into two segments. The low mode number region at the left contains most of the power and characterizes the gross structure. The positions of peaks in this region are a measure of the size of the structure, e.g. in Figure 21 there is a clear peak at a wavelength just under 0.5 km. This characterizes the typical widths of the fingers in Figure 6. The second region is the asymptotic regime, which begins, roughly speaking at a wavelength corresponding to the smallest scale size of the gross structure. This region can be fit approximately by a straight line (in the log of the power vs. the log of the mode number). The slope of that fit, N, is the asymptotic slope of the power spectrum. The value of the slope is determined by the steepest gradient in the field of view. A value of -2 corresponds to a square wave; steeper slopes to more gradual gradients. We have discarded the highest 15% of the modes

from this calculation since the highest modes are subject to severe 'aliasing' effects and to computational errors.⁽¹⁰⁾ The resolution we used (82 x 82) was dictated by the cost of the PHARO calculations and should be considered only marginally adequate. Thus, the values of N should be considered illustrative but not definitive. Figures 20 and 21 do indicate steeper gradients in the x direction than in the y direction.

We find that the steep gradients are established fairly early, certainly by 100 sec. However, as time proceeds the number of steep gradients increases. This shows up as an increase in the power level of this part of the spectrum, but with no change in slope. Since, as we have said, very little of the power is in the asymptotic part of the spectrum there need be very little change in the power spectrum at the lower modes to accommodate this increase.

From camera 2 we view along the x axis. Thus, the only power spectrum that is meaningful is the y power spectrum, in which the z components have been integrated over. The ion distribution in the z direction is strictly gaussian, and, thus, uninteresting. Figure 22 shows the y power spectrum from camera 2 at 140 sec at a distance of 200 km. Refer to Figure 13. While there is clearly mode structure here in the asymptotic region the value of N is not too different from that in Figure 21.

From camera 3 we view along the y axis. Only the x power spectrum, in which the z components have been integrated over, is of interest. Figure 23 shows the x power spectrum from camera 3

at 140 sec at a distance of 200 km. Refer to Figure 18. Again, there is a great deal of structure in the asymptotic region but the general falloff, characterized by the N value, is not too different from that in Figure 20.

c. Parallax Effects

Previous simulations⁽⁸⁾ have been two dimensional so that parallax effects were unobservable. We find that including the third dimension has a profound effect both on the radiance contours and on the irregularity spectral characteristics. We will illustrate this in two ways, by showing: (1) how these properties vary with distance and (2) how they vary with change in pointing direction.

Consider again camera 1 at 140 sec at a distance of 200 km, Figure 6, and compare with Figures 24 and 25, which are views from camera 1 at 140 sec at respectively 50 km and 600 km from the cloud. Clearly, at 50 km parallax has spread the contours greatly and substantially reduced the gradients. At 600 km the reverse has occurred and the gradients are larger. This is borne out by the power spectral results. Figures 26 and 27 are the x power spectra from, respectively, 50 km and 600 km and should be compared with Figure 20 for 200 km. The spectral index, N , at 50 km is -3.44, at 200 km is -2.90, and at 600 km is -2.39 documenting the clear sharpening of the steepest gradients as we recede from the cloud. Figures 28 and 29 are the y power spectra from, respectively, 50 km and 600 km which should be compared with

Figure 21 for 200 km. The y spectral index, N, is the same at 50 km and 200 km, within the accuracy of the fitting technique, but has decreased by $\approx 10\%$ at 600 km. This is because in the y direction there are steep gradients near the center of the field of view, where parallax effects are small, so that the steep gradients have been somewhat preserved. However, if we compare the power levels in the asymptotic regime at 50 km and 600 km, at some intermediate fixed wavenumber, we find the power down by about half a decade both in the x and y spectra (compare Figures 26 and 27 and Figures 28 and 29) at 50 km relative to 600 km. This is the best measure of the effect of parallax on the measured gradients.

Suppose now we imagine that camera 1, at 140 sec and a distance of 200 km, is rotated about the x axis by just 1° , toward camera 3. How does this affect the radiance contours? Figure 30 shows the resulting contours, which have been greatly spread out. Although the maximum radiance values have been reduced, compared to Figure 6, the irradiance at the camera is unchanged. As is obvious in Figure 30, the greatest change has occurred with the gradients in the y direction. The spectral index of the y power spectrum has increased from ~ -4 to ~ -7 .

Figure 31 shows the effect of rotating camera 1, about the y axis by 1° , toward the x axis. Here the changes from Figure 6 are moderate. However, the x power spectrum index does change from ~ -2.9 to ~ -5.5 and the y index increases by about 20%.

Thus, when we rotate toward the y direction we lose the y gradients and when we rotate toward the x direction we lose the x gradients.

V. SUMMARY

The severe degradation of radio signals due to structuring of electron densities in the atmosphere, following a HANE event, has been known for some years now. A great deal of analysis has been performed at the Naval Research Laboratory (NRL) to understand the plasma instability mechanisms that underlie this phenomenon, as well as related phenomena in the natural ionosphere, such as spread F. It is clear that these mechanisms also will result in structuring in the emission of LWIR radiation and consequently is potentially of serious concern to the U.S. defense community. Ultimately we want to use our theoretical understanding of striation phenomena along with our capabilities to simulate HANE phenomena using 3D magnetohydrodynamic computer models, to permit predictions of structuring following these events.

At present there is at issue the question of what, if any, sources of LWIR emission are likely to be most important in HANE events. The most likely candidates at present are (1) atomic oxygen and/or nitrogen recombination radiation and (2) LWIR emission from metallic oxides, such as uranium. To shed light on some of the unknowns in the second category DNA requires a reliable model of a hypothetical uranium release at high altitudes to clarify the emission wavelengths, intensities, and structuring. In this paper we have reported on the results of a numerical simulation of a uranium release at 200 km in daylight, making reasonable assumptions about

the values for some of the unknown parameters. We have presented contour plots of radiance in the 11-14 μ region of the LWIR as it would be observed from detectors placed at various locations along and transverse to the magnetic field and at various distances from the cloud.

This enables us to observe the development in time of the radiance from the cloud as it would appear from any vantage point of interest. We see clearly the steepening of the cloud, the development of fingering, and how this is related to the power spectral characteristics that are observed. Most importantly, we have shown that the three dimensional nature of the cloud has a profound effect on the radiance contours and on the observed spectral characteristics. Being stationed closer or observing slightly off axis can greatly reduce the gradients in the radiance of the cloud and change the power spectral characteristics accordingly. The results of our simulation should provide a theoretical understanding of a hypothetical experimental release. It should also be recognized that the simulations we have presented are a first cut, i.e., of a preliminary nature. Clearly, improvements in the numerical simulations presented here will be made. Nevertheless, these simulations provide some interesting results on structuring in the LWIR regime.

ACKNOWLEDGMENT

This work was supported by the Defense Nuclear Agency. We would like to thank Professor N. J. Zabusky for useful discussions on obtaining the power spectra from the PHARO plots.

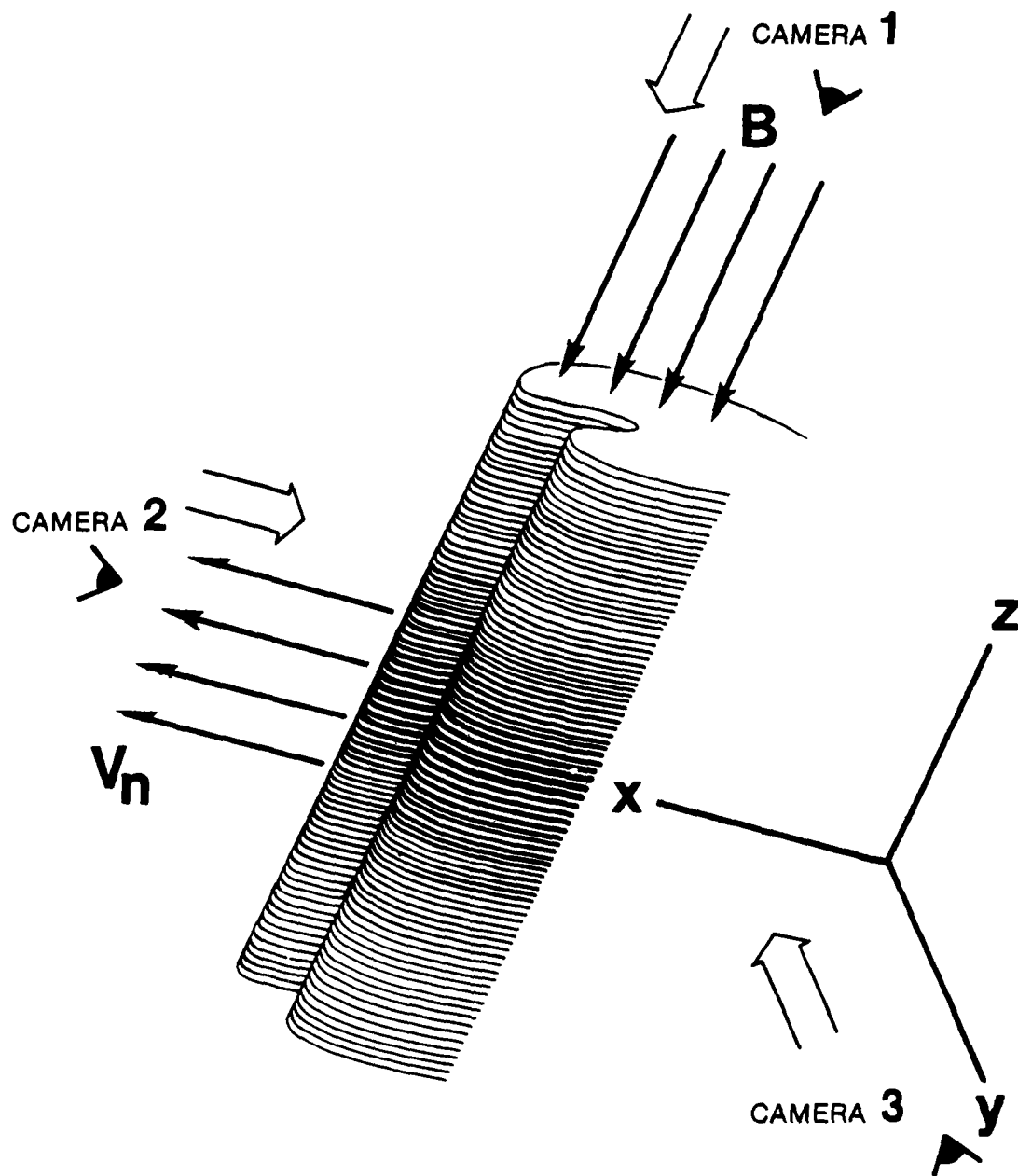


Fig. 1 - Schematic view of the uranium cloud and the coordinate system, showing diffusion along the magnetic field, and striation formation across the direction of the neutral-ion relative velocity direction v_n . Locations of the cameras discussed in the text are indicated.

CAMERA 1 T(SEC) 6.0110E 01
 0.39 CONTOURS 0.00E 00 1.12E-07 1.25E-08

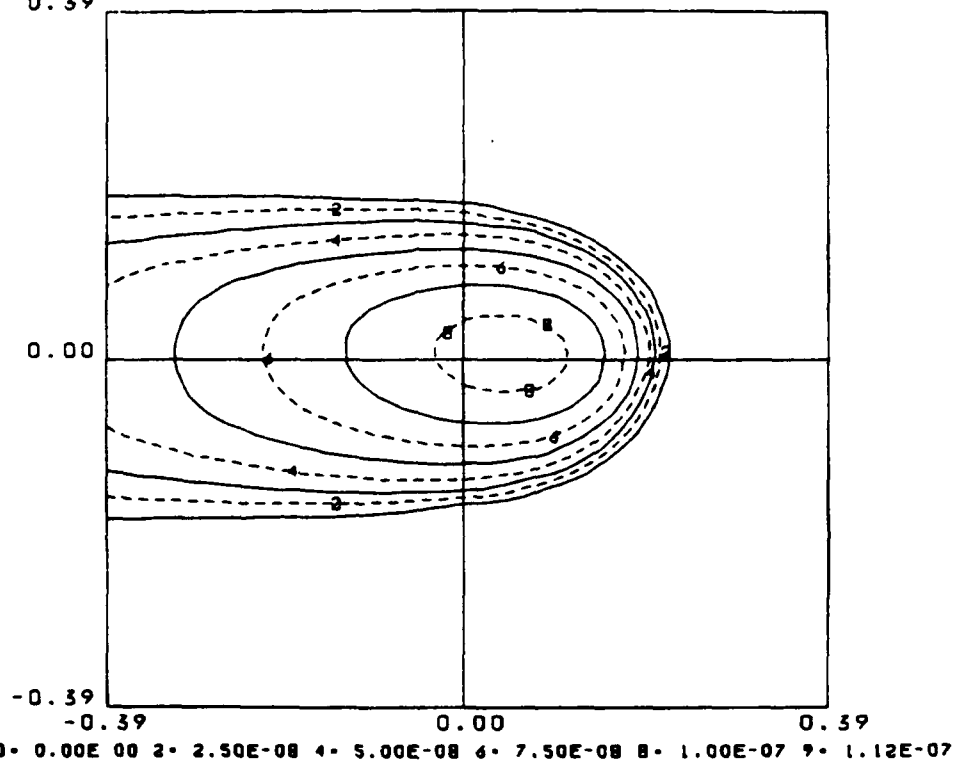


Fig. 2 - Camera 1 radiance contours (watts/cm²ster) 200 km from the cloud origin, 60 sec after release. Abscissa and ordinate are in degrees. Refer to text for contour label values or to key at bottom.

CAMERA 1 T(SEC) 8.0114E 01
 0.39 CONTOURS 0.00E 00 1.12E-07 1.25E-08

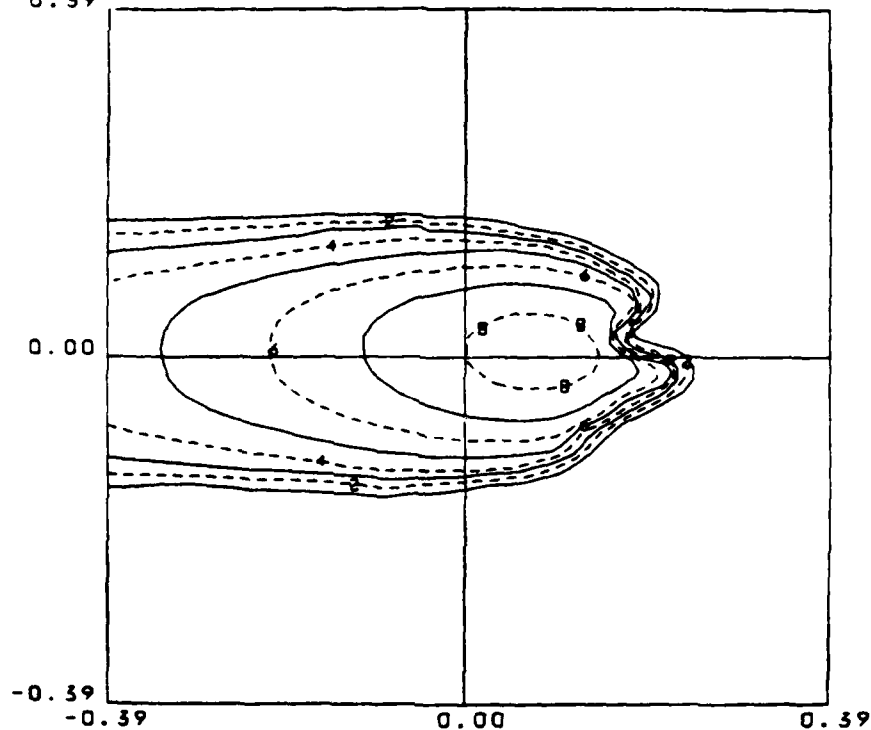


Fig. 3 - Camera 1 radiance contours (watts/cm² ster) 200 km from the cloud origin, 80 sec after release. Abscissa and ordinate are in degrees. Refer to text for contour label values or to key at bottom.

CAMERA 1 T(SEC) 1.0007E 02
 0.39 CONTOURS 0.00E 00 1.12E-07 1.25E-08

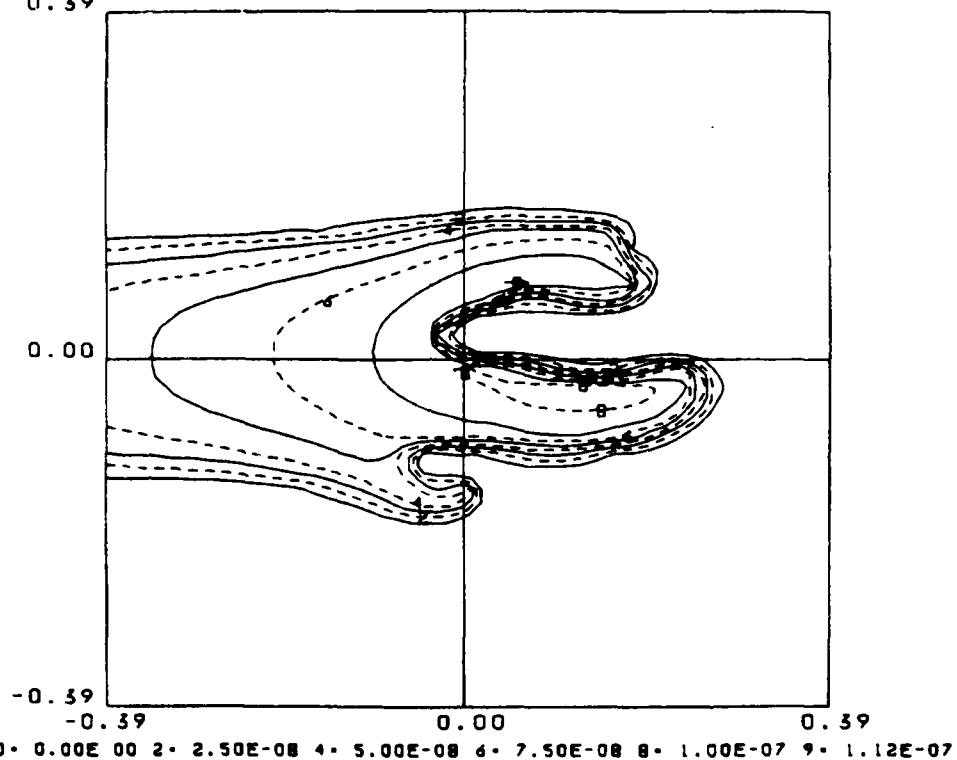


Fig. 4 - Camera 1 radiance contours (watts/cm² ster) 200 km from the cloud origin, 100 sec after release. Abscissa and ordinate are in degrees. Refer to text for contour label values or to key at bottom.

CAMERA 1 T(SEC) 1.2007E 02
 0.39 CONTOURS 0.00E 00 1.12E-07 1.25E-08

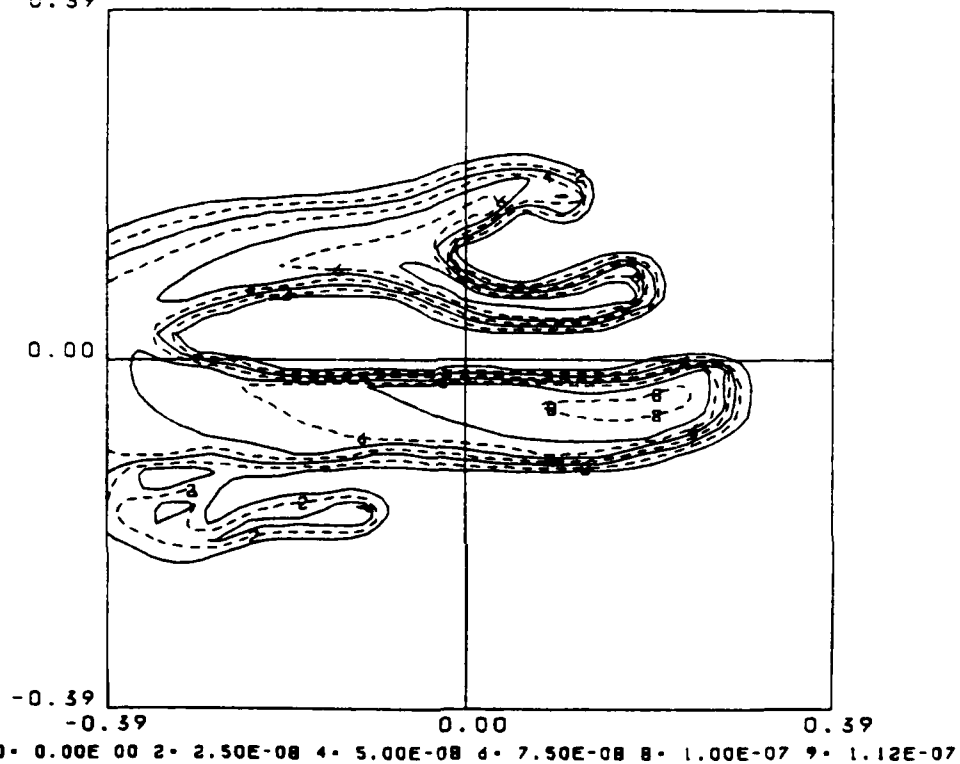


Fig. 5 - Camera 1 radiance contours (watts/cm²ster) 200 km from the cloud origin, 120 sec after release. Abscissa and ordinate are in degrees. Refer to text for contour label values or to key at bottom.

CAMERA 1 T(SEC) 1.4005E 02
 0.39 CONTOURS 0.00E 00 1.12E-07 1.25E-08

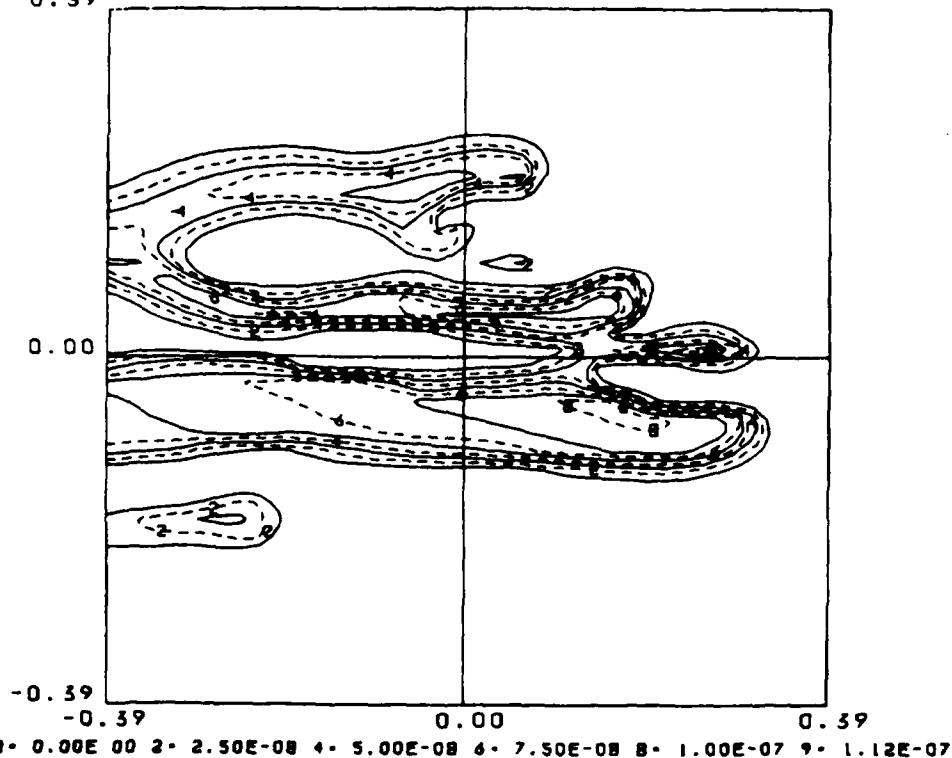


Fig. 6 - Camera 1 radiance contours (watts/cm²ster) 200 km from the cloud origin, 140 sec after release. Abscissa and ordinate are in degrees. Refer to text for contour label values or to key at bottom.

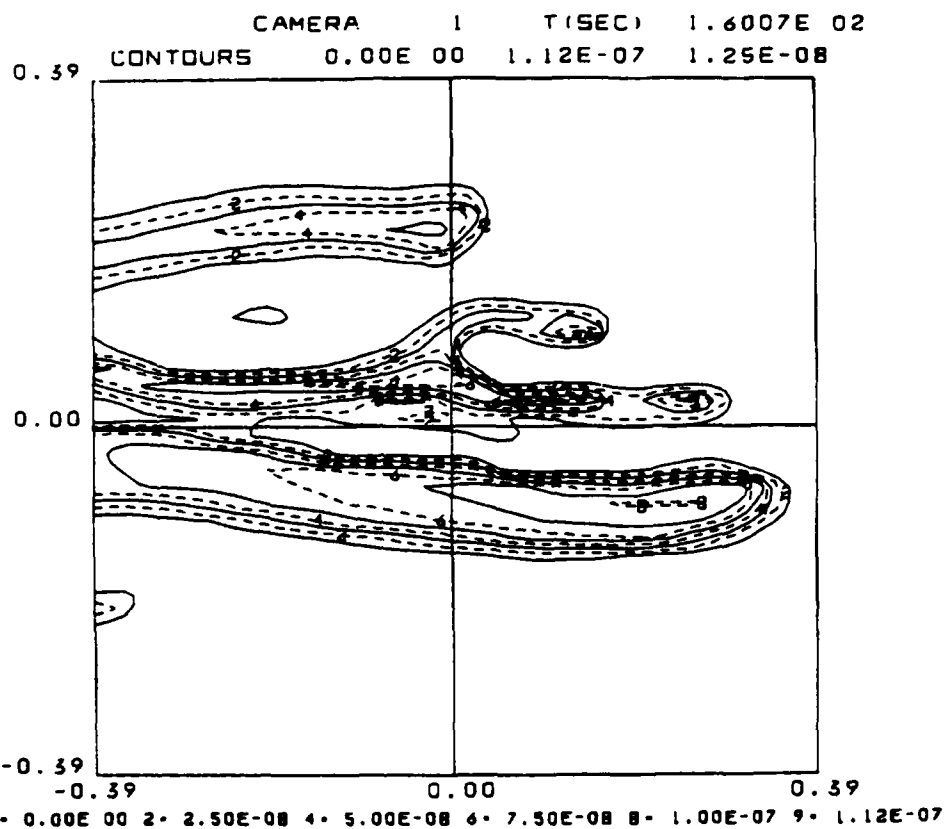


Fig. 7 - Camera 1 radiance contours ($\text{watts/cm}^2 \text{ster}$) 200 km from the cloud origin, 160 sec after release. Abscissa and ordinate are in degrees. Refer to text for contour label values or to key at bottom.

CAMERA 1 T(SEC) 1.8002E 02
 0.39 CONTOURS 0.00E 00 1.12E-07 1.25E-08

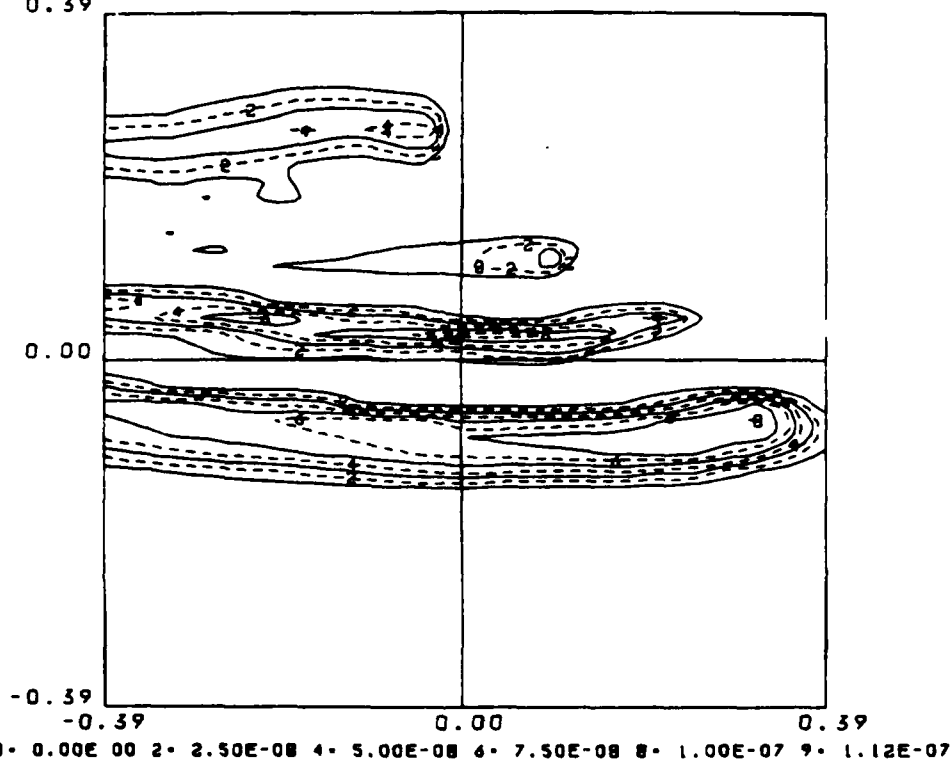


Fig. 8 - Camera 1 radiance contours ($\text{watts/cm}^2 \text{ster}$) 200 km from the cloud origin, 180 sec after release. Abscissa and ordinate are in degrees. Refer to text for contour label values or to key at bottom.

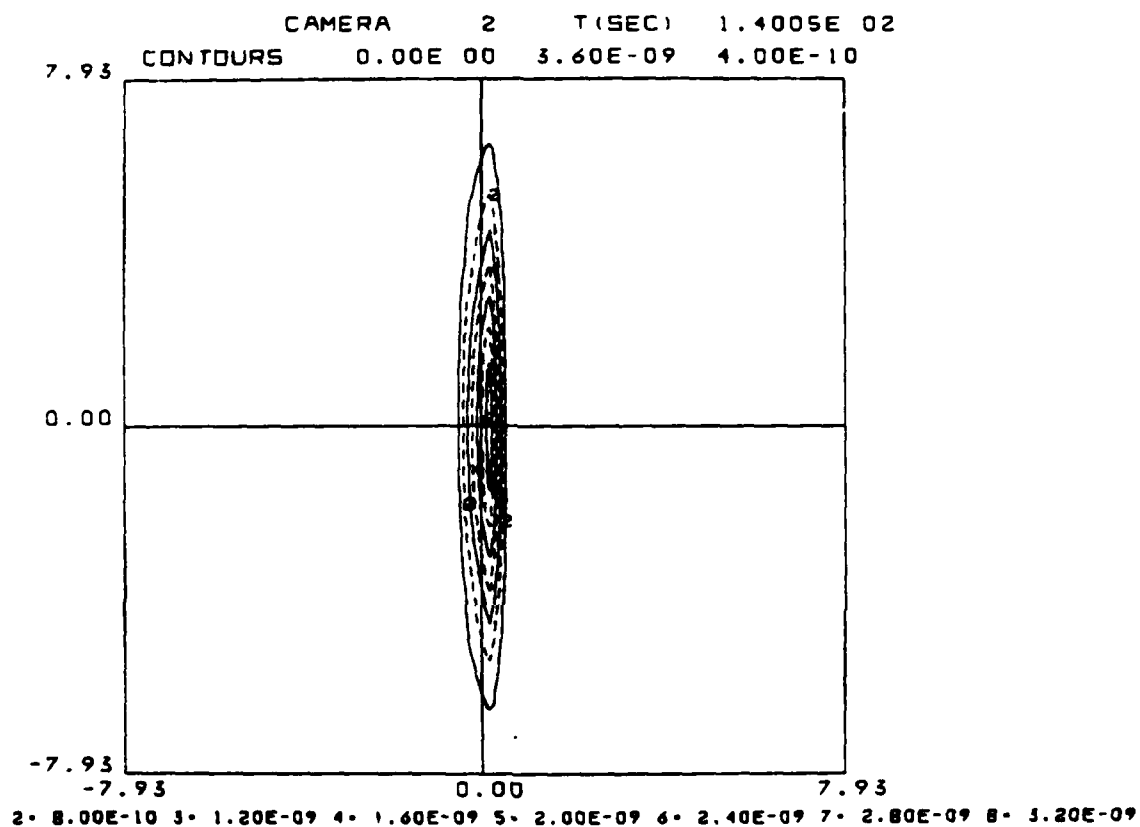


Fig. 9 - Camera 2 radiance contours ($\text{watts/cm}^2 \text{ster}$) 200 km from the cloud origin, 140 sec after release. Abscissa and ordinate are in degrees. This camera view has a large field of view so that the entire extent of the cloud is evident. Refer to text for contour label values or to key at bottom.

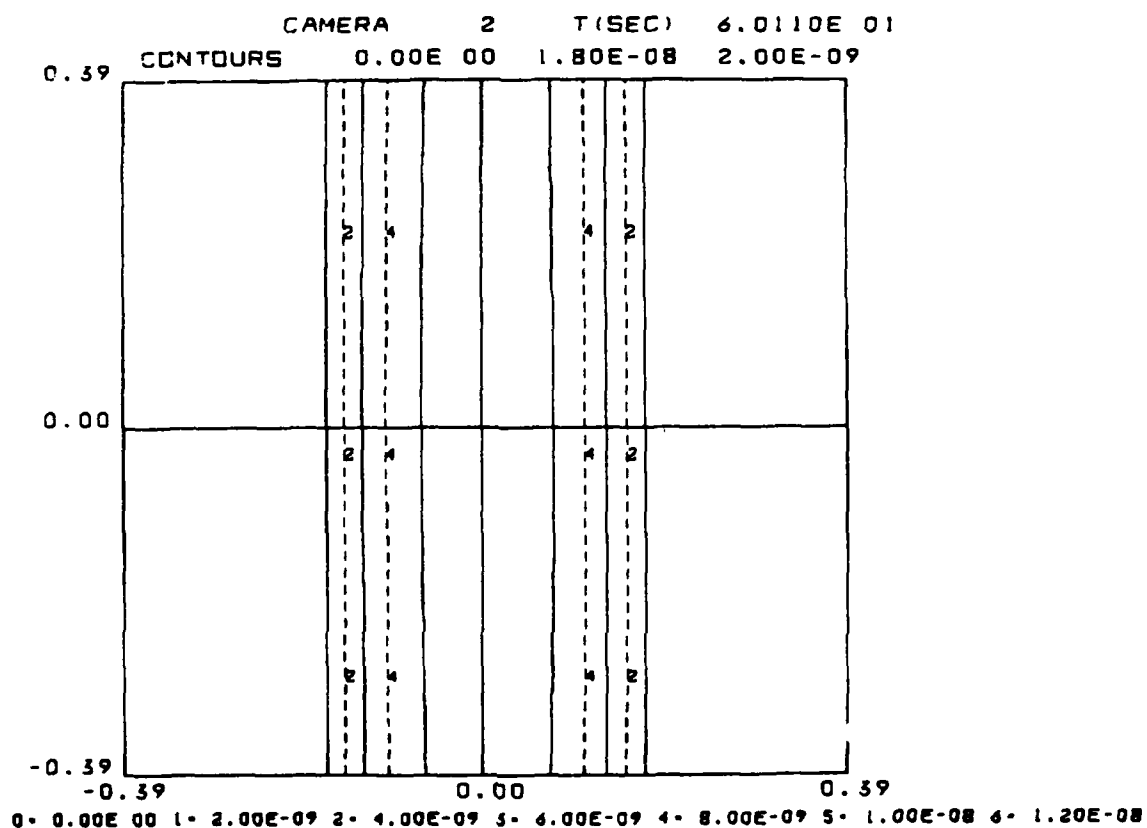


Fig. 10 - Camera 2 radiance contours (watts/cm²ster) 200 km from the cloud origin, 60 sec after release. Abscissa and ordinate are in degrees. Refer to contour label values in text or to key at bottom.

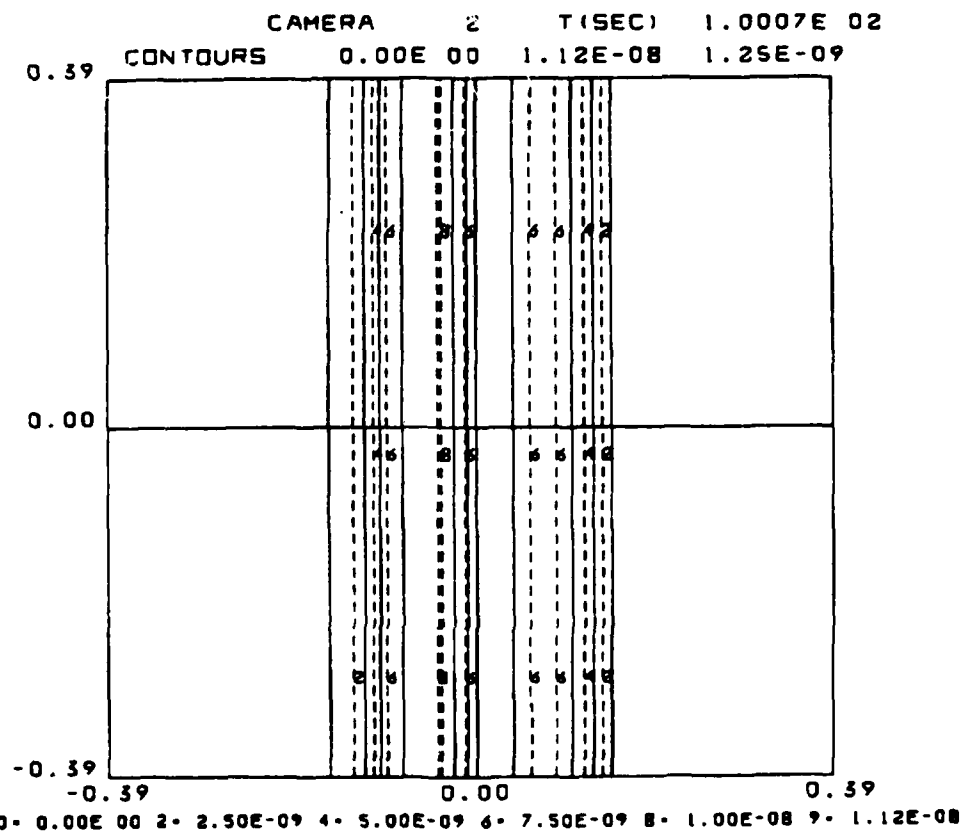


Fig. 11 - Camera 2 radiance contours ($\text{watts/cm}^2 \text{ster}$) 200 km from the cloud origin, 100 sec after release. Abscissa and ordinate are in degrees. Refer to contour label values in text or to key at bottom.

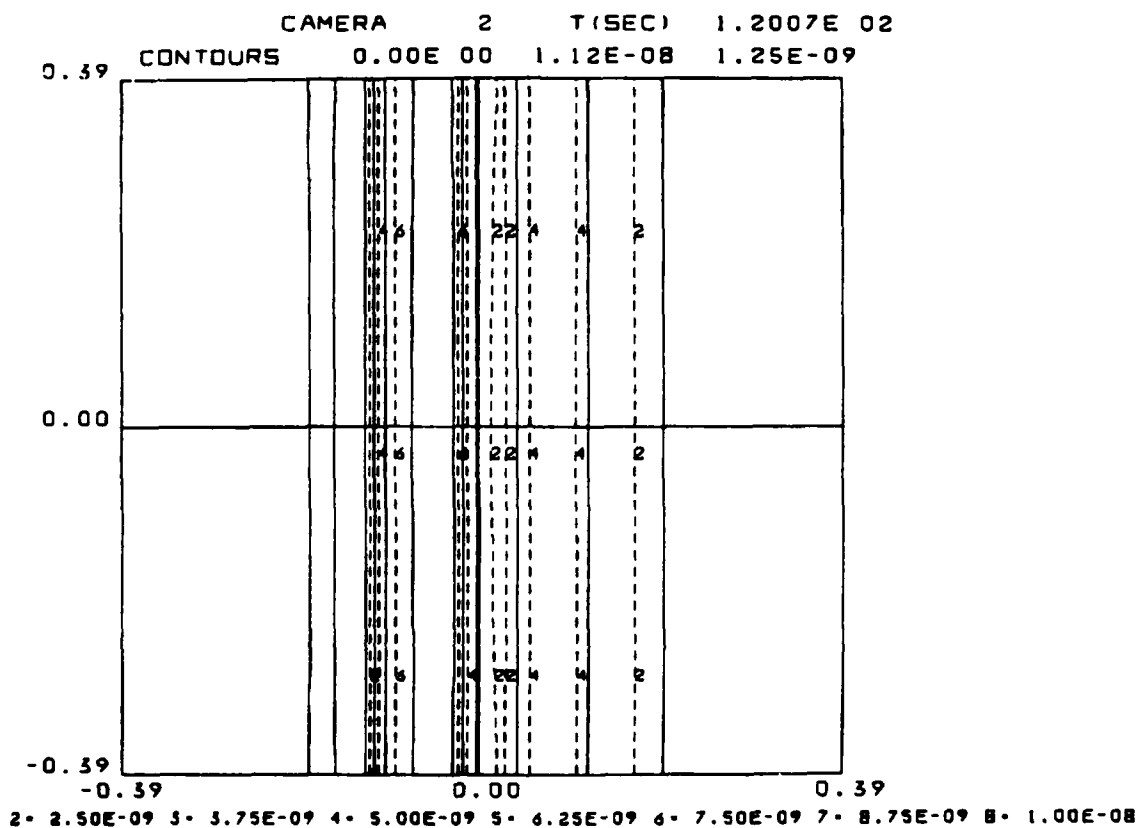


Fig. 12 - Camera 2 radiance contours ($\text{watts/cm}^2 \text{ster}$) 200 km from the cloud origin, 120 sec after release. Abscissa and ordinate are in degrees. Refer to contour label values in text or to key at bottom.

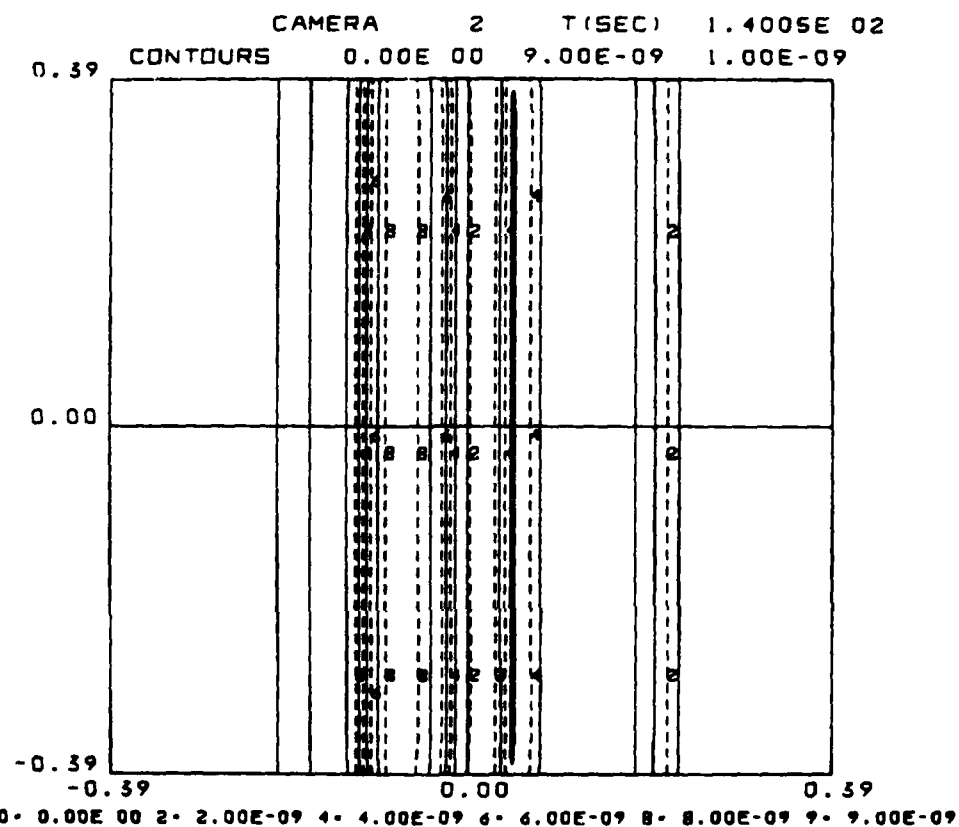


Fig. 13 - Camera 2 radiance contours ($\text{watts/cm}^2\text{ster}$) 200 km from the cloud origin, 140 sec after release. Abscissa and ordinate are in degrees. Refer to contour label values in text or to key at bottom.

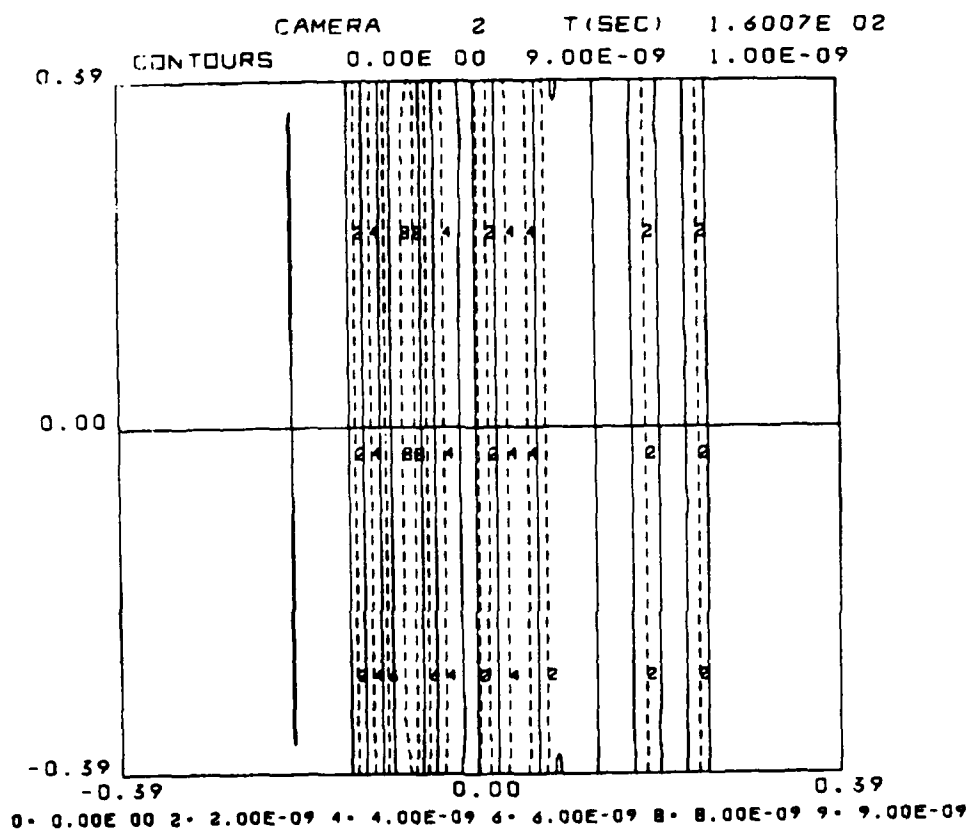


Fig. 14 - Camera 2 radiance contours ($\text{watts/cm}^2 \text{ster}$) 200 km from the cloud origin, 160 sec after release. Abscissa and ordinate are in degrees. Refer to contour label values in text or to key at bottom.

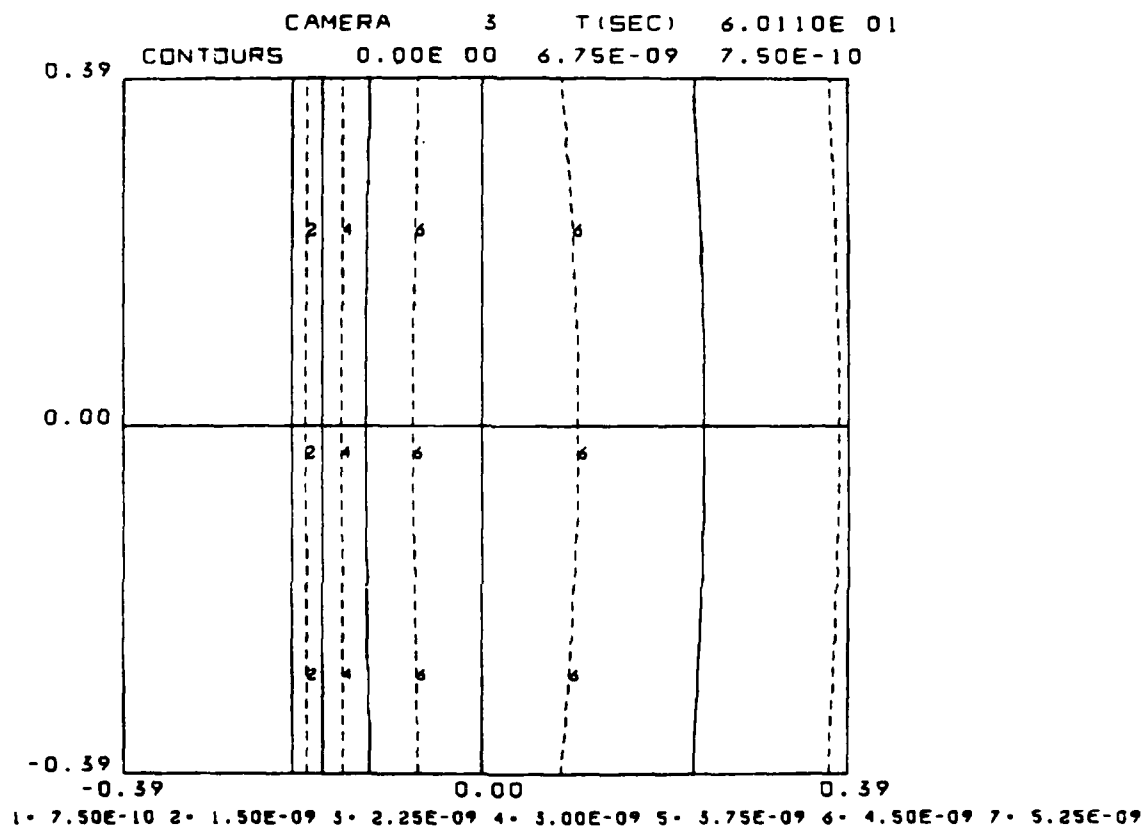


Fig. 15 - Camera 3 radiance contours (watts/cm² ster) 200 km from the cloud origin, 60 sec after release. Abscissa and ordinate are in degrees. Refer to contour label values in text or to key at bottom.

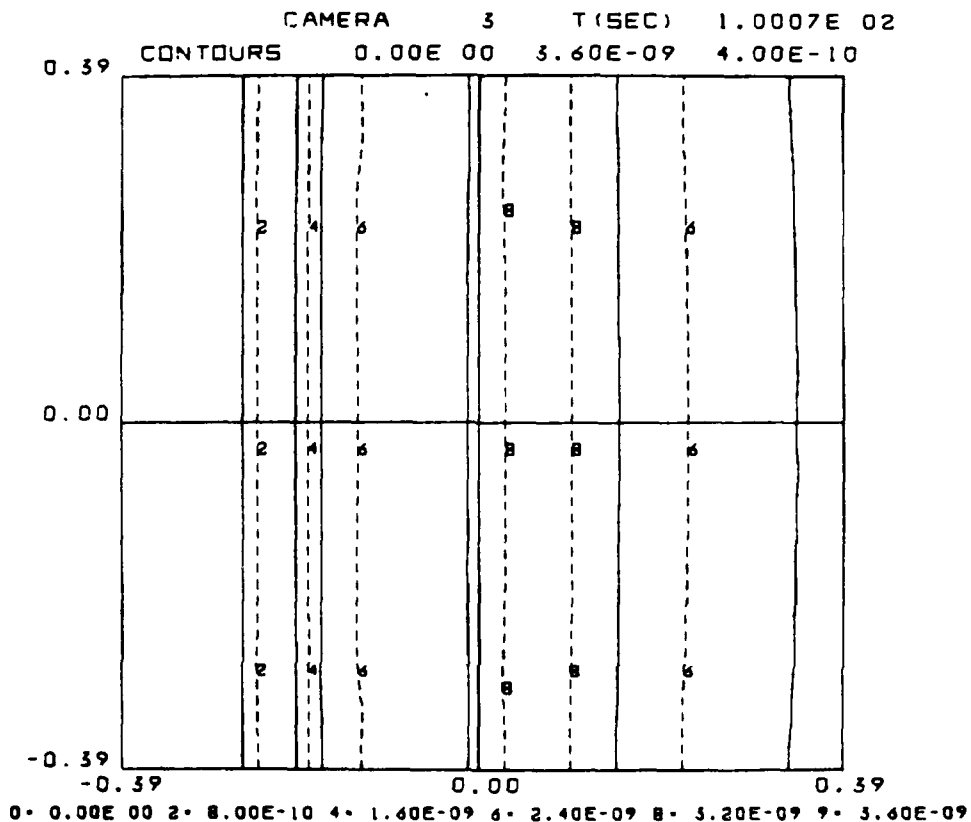


Fig. 16 - Camera 3 radiance contours (watts/cm² ster) 200 km from the cloud origin, 100 sec after release. Abscissa and ordinate are in degrees. Refer to contour label values in text or to key at bottom.

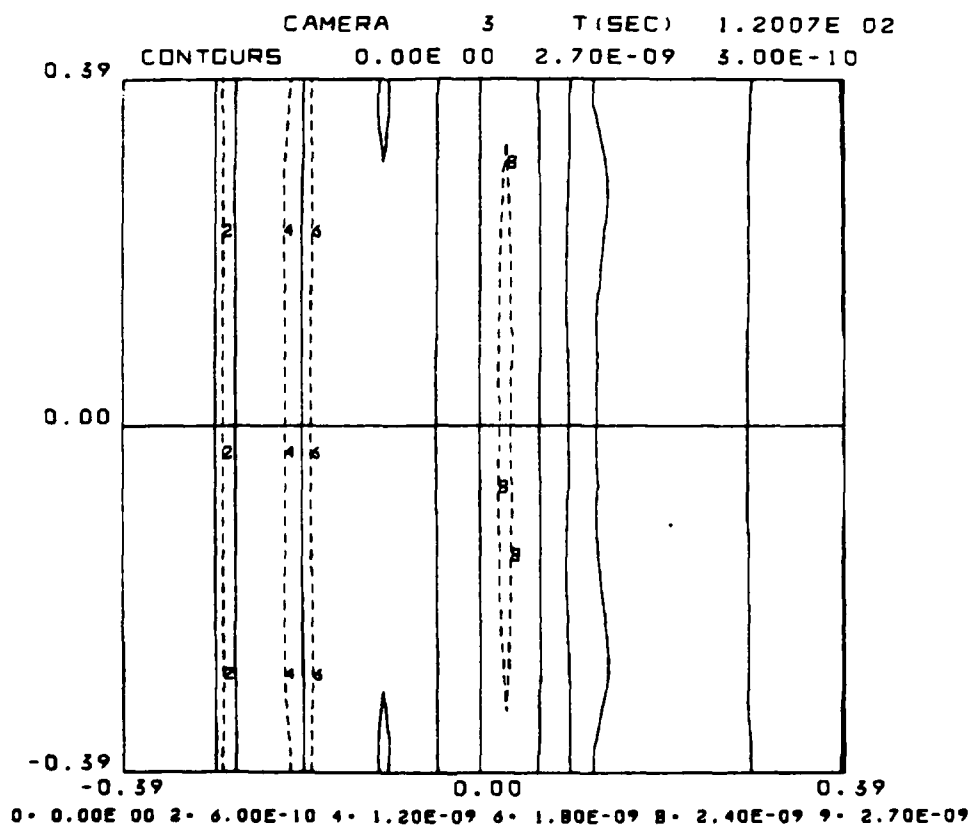


Fig. 17 - Camera 3 radiance contours (watts/cm²ster) 200 km from the cloud origin, 120 sec after release. Abscissa and ordinate are in degrees. Refer to contour label values in text or to key at bottom.

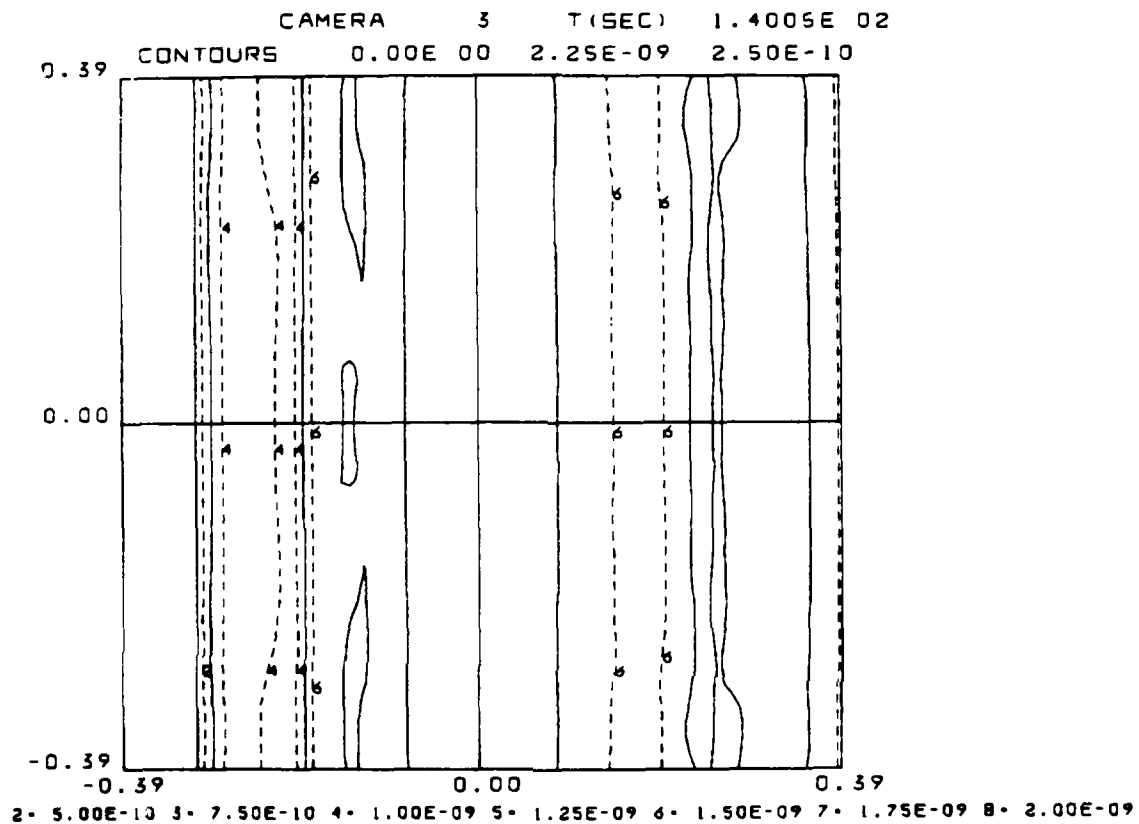


Fig. 18 - Camera 3 radiance contours ($\text{watts/cm}^2 \text{ster}$) 200 km from the cloud origin, 140 sec after release. Abscissa and ordinate are in degrees. Refer to contour label values in text or to key at bottom.

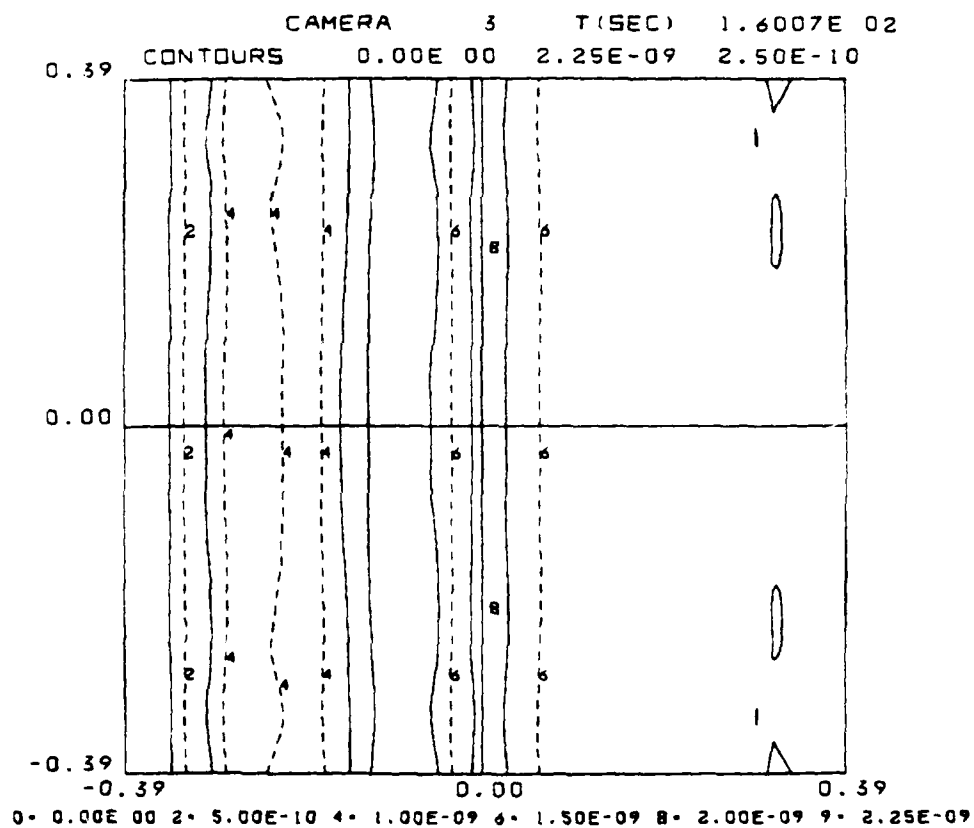


Fig. 19 - Camera 3 radiance contours ($\text{watts/cm}^2\text{ster}$) 200 km from the cloud origin, 160 sec after release. Abscissa and ordinate are in degrees. Refer to contour label values in text or to key at bottom.

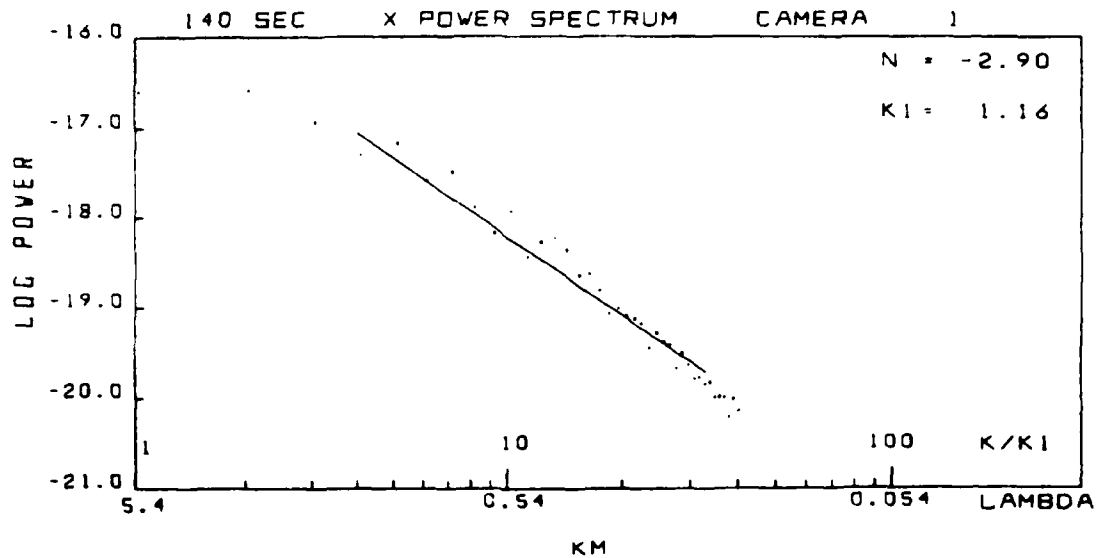


Fig. 20 - x Power spectrum from camera 1 (Figure 6 field of view).
Refer to text for explanation of scales.

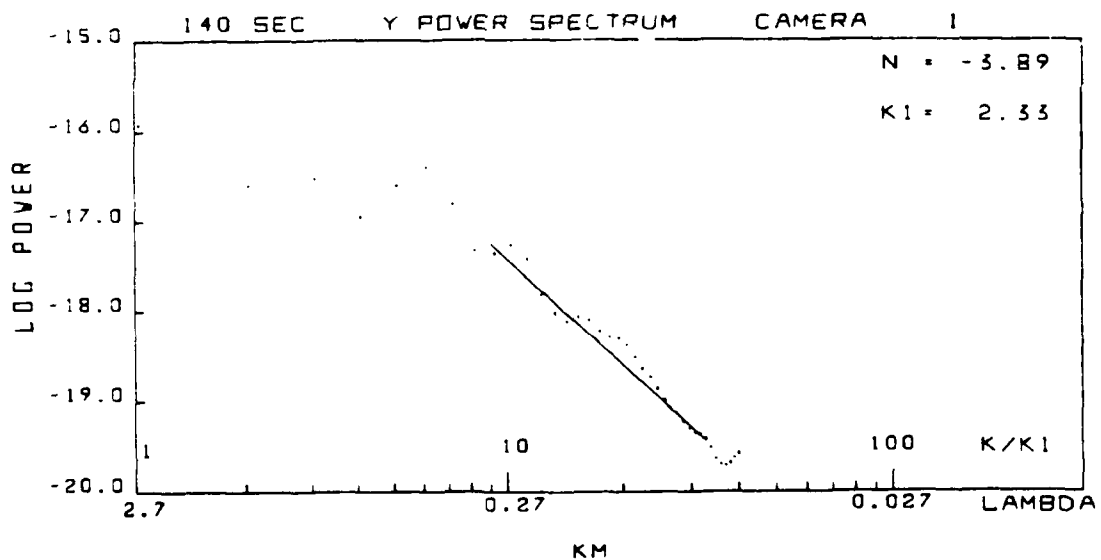


Fig. 21 - y Power spectrum from camera 1 (Figure 6 field of view).
Refer to text for explanation of scales.

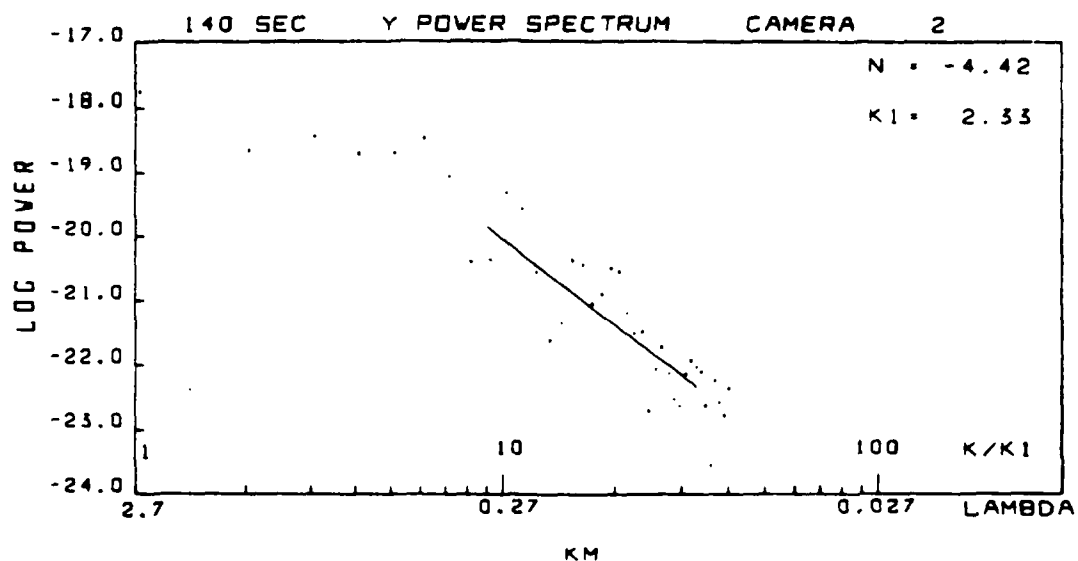


Fig. 22 - y Power spectrum from camera 2 (Figure 13 field of view).
Refer to text for explanation of scales.

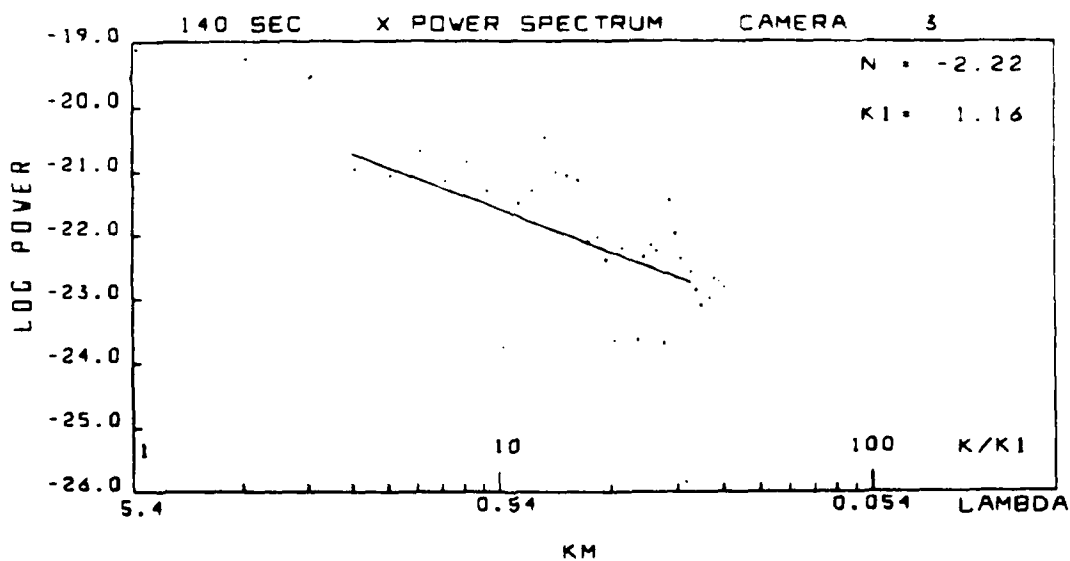


Fig. 23 - x Power spectrum from camera 3 (Figure 18 field of view).
Refer to text for explanation of scales.

CAMERA 1 (50 km) T(SEC) 1.4005E 02
 1.57 CONTOURS 0.00E 00 1.12E-07 1.25E-08

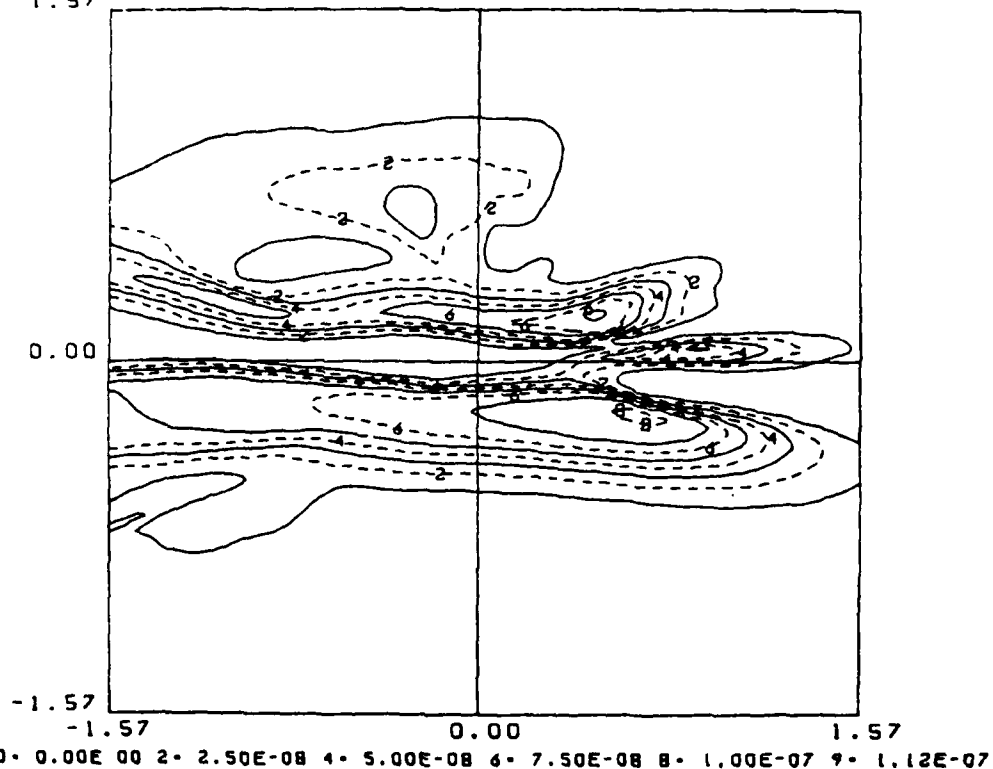


Fig. 24 - Camera 1 radiance contours (watts/cm² ster) 50 km from the cloud origin, 140 sec after release. Abscissa and ordinate are in degrees. Refer to text for contour label values or to key at bottom.

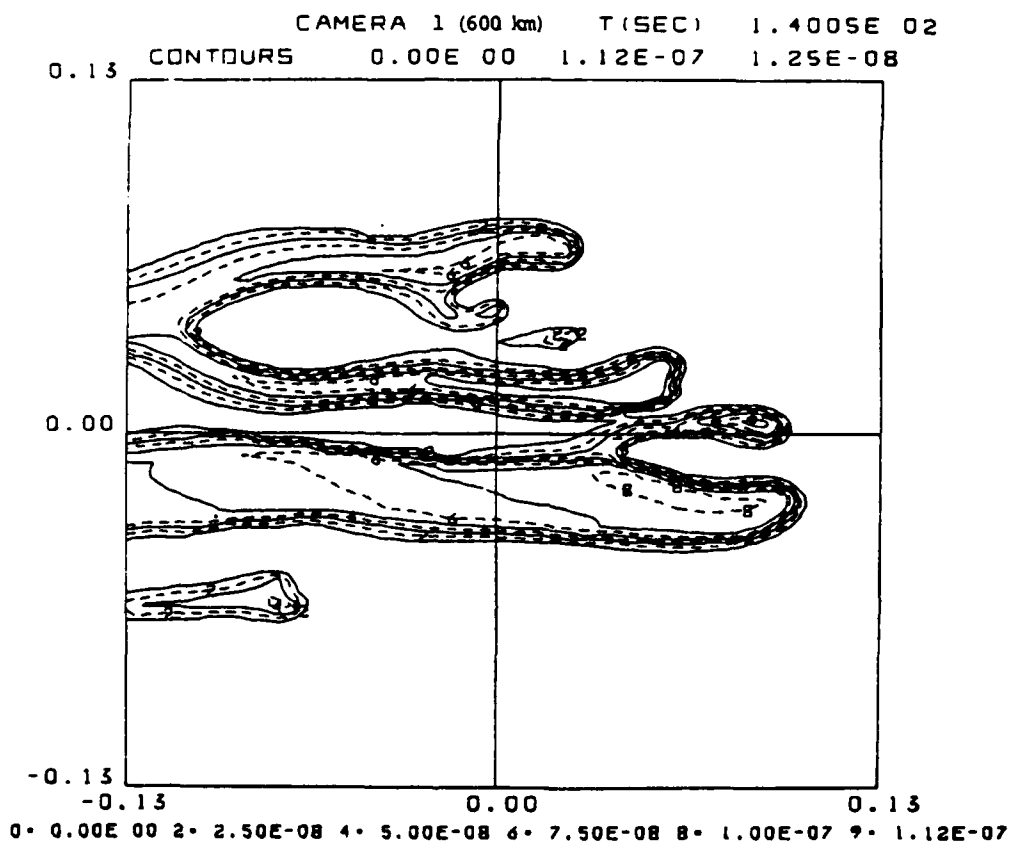


Fig. 25 - Camera 1 radiance contours (watts/cm²ster) 600 km from the cloud origin, 140 sec after release. Abscissa and ordinate are in degrees. Refer to text for contour label values or to key at bottom.

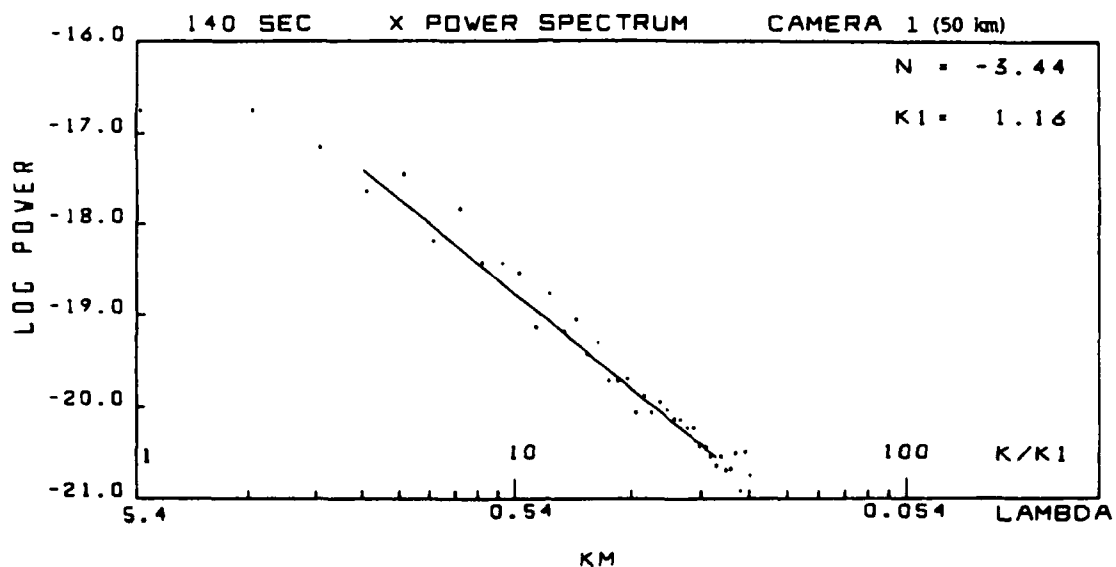


Fig. 26 - x Power spectrum from camera 1 (Figure 24 field of view).
Refer to text for explanation of scales.

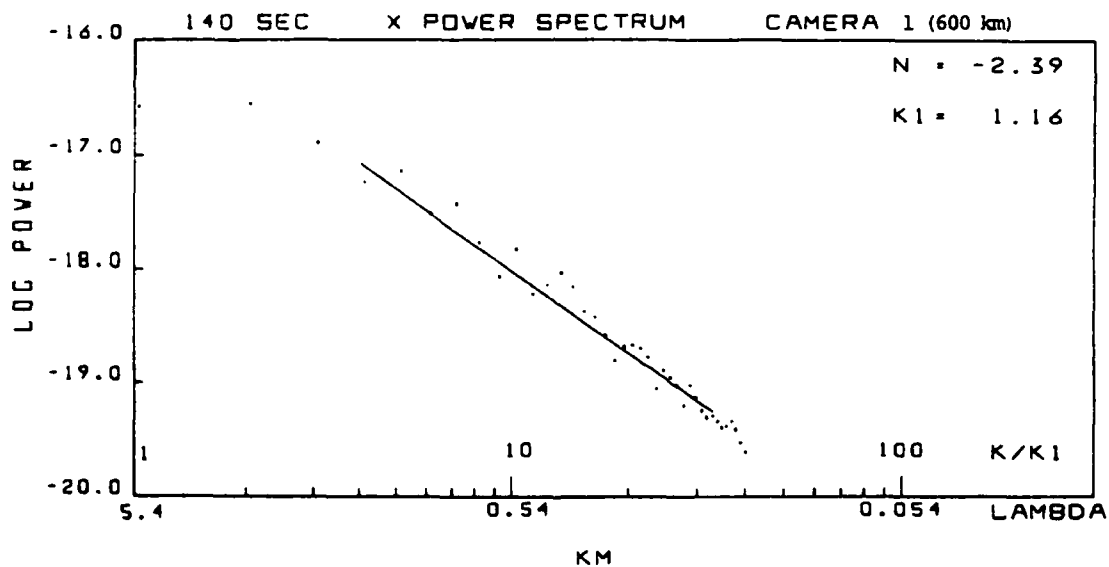


Fig. 27 - x Power spectrum from camera 1 (Figure 25 field of view).
Refer to text for explanation of scales.

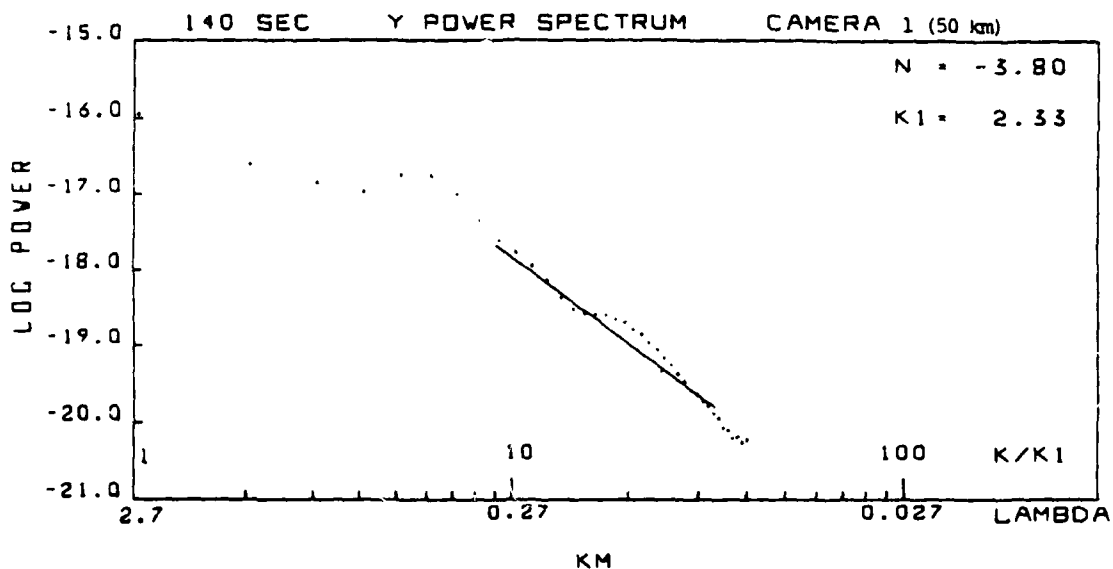


Fig. 28 - y Power spectrum from camera 1 (Figure 24 field of view).
Refer to text for explanation of scales.

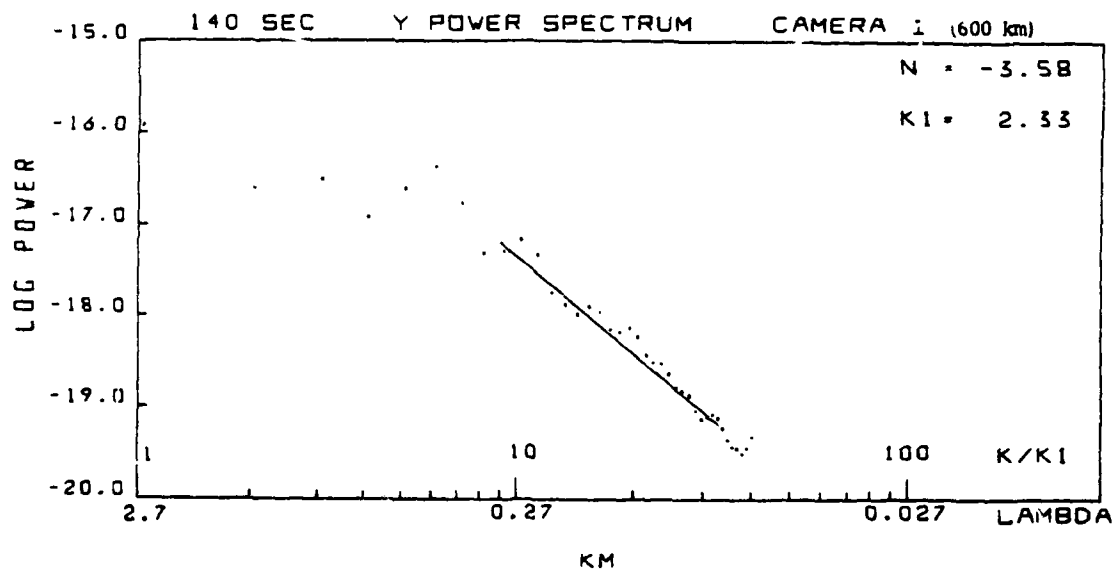


Fig. 29 - y Power spectrum from camera 1 (Figure 25 field of view).
Refer to text for explanation of scales.

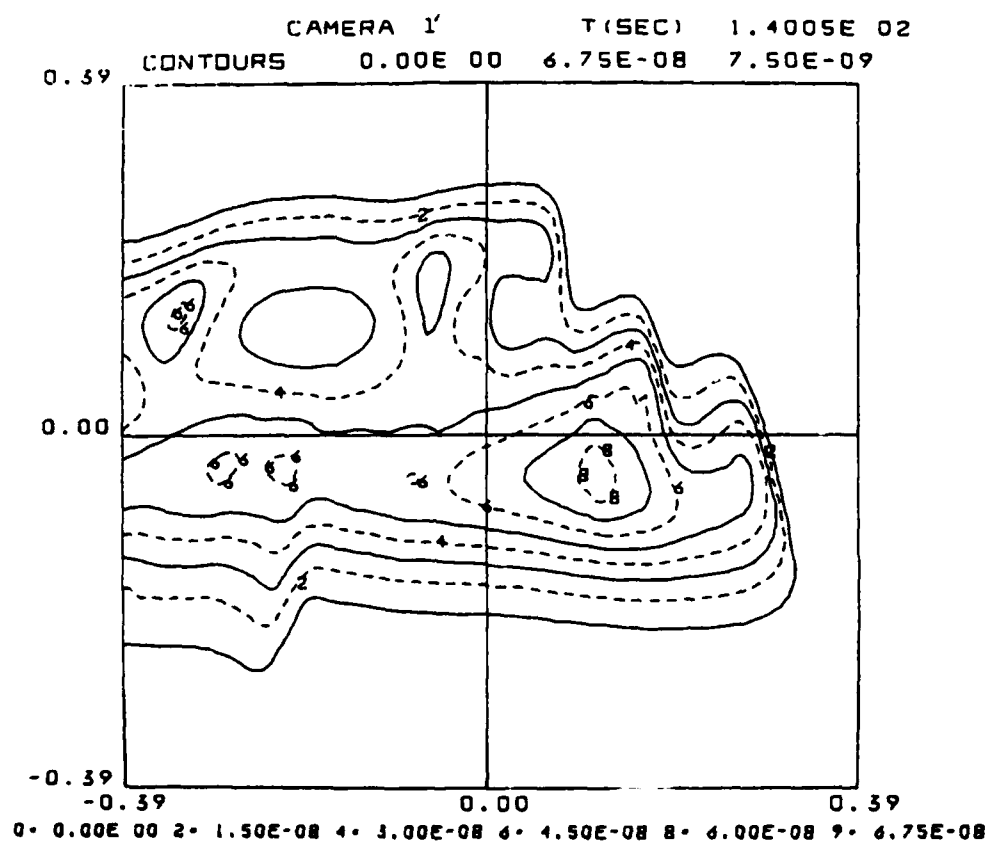


Fig. 30 - Camera 1, rotated 1° about x axis toward camera 3, radiance contours (watts/cm²ster) 200 km from the cloud origin, 140 sec after release. Abscissa and ordinate are in degrees. Refer to text for contour label values or to key at bottom.

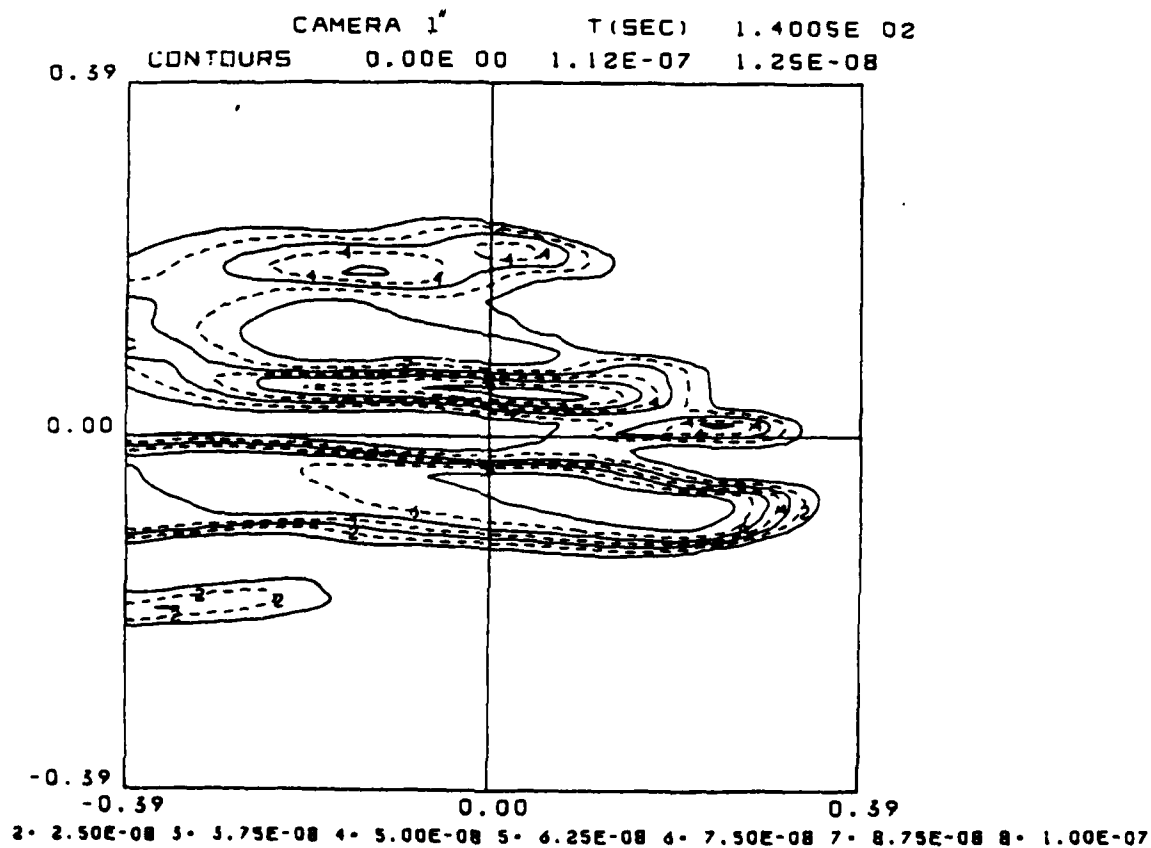


Fig. 31 - Camera 1, rotated 1° about y axis toward camera 2, radiance contours (watts/cm²ster) 200 km from the cloud origin, 140 sec after release. Abscissa and ordinate are in degrees. Refer to text for contour label values or key at bottom.

REFERENCES

1. Bien, F., "Nitric Oxide and Uranium Oxide Ion Studies", AFGL-TR-79-0164, June 1979.
2. Reidy, W.P., "LWIR/Structured Release Characteristics", Proceedings of the DNA Infrared Program Meeting, 23-24 January 1980.
3. Fite, W.L., T.A. Patterson, and M.W. Siegel, "Cross-Sections for Thermal Reactions Between Uranium Atoms and Atmospheric Species", AFGL TR77-0029, (1977).
4. Ossakow, S.L. and P.K. Chaturvedi, "Morphological Studies of Rising Equatorial Spread F Bubbles", J. Geophys. Res. 83, 2085 (1978).
5. Fite, W.L. and H.H. Lo, "Reactions of UO^+ with Atmospheric Gases", AFGL TR77-0029 (1977).
6. Gilmore, F., "Metal Oxides", Proceedings of the DNA Infrared Program Meeting, 23-24 January 1980.
7. Reidy, W.P., private communication.
8. McDonald, B.E., M.J. Keskinen, S.L. Ossakow, and S.T. Zalesak, "Computer Simulation of Gradient Drift Instability Processes in Operation Avefria", J. Geophys. Res. 85, 2145 (1980).
9. Hyman, E., M. Mulbrandon, and S. Ossakow, "The PHARO Code", NRL Memorandum Report 4667 (1981).
10. Labusky, N.J. and J. Block, "Estimating the Spectrum of Electron Density Fluctuations from Simulations of Ionospheric Plasma Clouds", NRL Memorandum Report 3586, July 1978.

DISTRIBUTION LIST

DEPARTMENT OF DEFENSE

DIRECTOR
DEFENSE NUCLEAR AGENCY
WASHINGTON, D.C. 20305
04CY ATTN TITL
01CY ATTN DDST
03CY ATTN RAAE

COMMANDER/DIRECTOR
ATMOSPHERIC SCIENCES LABORATORY
U.S. ARMY ELECTRONICS COMMAND
WHITE SANDS MISSILE RANGE, NM 88002
01CY ATTN DELAS-EO F. NILES

DIRECTOR
BMD ADVANCED TECH CTR
HUNTSVILLE OFFICE
P. O. BOX 1500
HUNTSVILLE, AL 35807
01CY ATTN ATC-T MELVIN T. CAPPS
01CY ATTN ATC-O W. DAVIES
01CY ATTN ATC-R DON RUSS

COMMANDER
BMD SYSTEMS COMMAND
P. O. BOX 1500
HUNTSVILLE, AL 35807
01CY ATTN R. DEKALB

DIRECTOR
NAVAL RESEARCH LABORATORY
WASHINGTON, D.C. 20375
01CY ATTN CODE 4700 T.P. COFFEY
(26 CYS IF UN. 1 CY IF CLASS)
01CY ATTN CODE 4701 JACK D. BROWN
01CY ATTN CODE 4780 BRANCH HEAD
(150 CYS IF UN. 1 CY IF CLASS)

AIR FORCE GEOPHYSICS LABORATORY
HANSCOM AFB, MA 01731
01CY ATTN OPR HAROLD GARDNER
01CY ATTN LKB KENNETH S. W. CHAMPION
01CY ATTN OPR ALVA T. STAIR
01CY ATTN OPR RUSS ARMSTRONG

LOS ALAMOS SCIENTIFIC LABORATORY
P. O. BOX 1663
LOS ALAMOS, NM 87545
01CY ATTN DOC CON FOR T. BINIEWSKI
01CY ATTN DOC CON FOR R. JEFFRIES
01CY ATTN DOC CON FOR G. STREIT
01CY ATTN DOC CON FOR J. ZINN

DEPARTMENT OF COMMERCE
NATIONAL BUREAU OF STANDARDS
WASHINGTON, D. C. 20234
(ALL CORRES: ATTN SEC OFFICE FOR)
01CY ATTN M. KRAUSS

NATIONAL OCEANIC & ATMOSPHERIC ADMIN
ENVIRONMENTAL RESEARCH LABORATORIES
DEPARTMENT OF COMMERCE
BOULDER, CO 80302
01CY ATTN F. FEHSENFELD

BERKELEY RESEARCH ASSOCIATES, INC.
P. O. BOX 983
BERKELEY, CA 94701
01CY ATTN J. WORKMAN

KAMAN TEMPO
816 STATE STREET (P.O. DRAWER 000)
SANTA BARBARA, CA 93102
01CY ATTN DASIAC
01CY ATTN TIM STEPHANS
01CY ATTN WARREN S. KNAPP
01CY ATTN WILLIAM MCNAMARA
01CY ATTN MACK STANTON

GENERAL RESEARCH CORPORATION
SANTA BARBARA DIVISION
P. O. Box 6770
SANTA BARBARA, CA 93111
01CY ATTN JOHN ISE, JR.
01CY ATTN JOEL GARBARINO

INSTITUTE FOR DEFENSE ANALYSES
400 ARMY-NAVY DRIVE
ARLINGTON, VA 22202
01CY ATTN ERNEST BAUER
01CY ATTN HANS WOLFHARD

R & D ASSOCIATES
P. O. BOX 9695
MARINA DEL REY, CA 92091
01CY ATTN FORREST GILMORE
01CY ATTN BRYAN GABBARD
01CY ATTN ROBERT F. LELEVIER

SCIENCE APPLICATIONS, INC.
P. O. BOX 2351
LA JOLLA, CA 92038
01CY ATTN DANIEL A. HAMLIN

MCDONNELL DOUGLAS CORPORATION
5301 BOLSA AVENUE
HUNTINGTON BEACH, CA 92647
01CY ATTN R. W. HALPRIN

MISSION RESEARCH CORPORATION
735 STATE STREET
SANTA BARBARA, CA 93101
01CY ATTN D. SAPPENFIELD
01CY ATTN R. BOGUSCH
01CY ATTN R. HENDRICK
01CY ATTN RALPH KILB
01CY ATTN DAVE SOWLE
01CY ATTN F. FAJEN
01CY ATTN M. SCHEIBE

PHOTOMETRICS, INC.
442 MARRETT ROAD
LEXINGTON, MA 02173
01CY ATTN IRVING L. KOFSKY

TECHNOLOGY INTERNATIONAL CORP.
75 WIGGINS AVENUE
BEDFORD, MA 01730
01CY ATTN W. P. BOQUIST

SRI INTERNATIONAL
333 RAVENSWOOD AVENUE
MENLO PARK, CA 94025
01CY ATTN WALTER G. CHESNUT
01CY ATTN CHARLES L. RINO
01CY ATTN R. HAKE, JR.
01CY ATTN D. MCDANIEL

UNITED TECHNOLOGIES RESEARCH CENTER
EAST HARTFORD CT 06108
01CY ATTN H. MICHAELS

AERODYNE
BEDFORD RESEARCH PARK
BEDFORD, MA 01730
01CY ATTN C. KOLB

STEWART RADIANCE LABORATORY
UTAH STATE UNIVERSITY
1 DEANGELO DRIVE
BEDFORD, MA 01730
01CY ATTN J. ULWICK

VISIDYNE, INC.
5 CORPORATE PLACE
SO. BEDFORD STREET
BURLINGTON, MA 01803
01CY ATTN W. REIDY
01CY ATTN J. CARPENTER
01CY ATTN C. HUMPHREY